

Testing an indirect method for identifying galaxies with high levels of Lyman continuum leakage

Satoshi Yamanaka^{1,2,★}, Akio K. Inoue^{1,2,3}, Toru Yamada⁴, Erik Zackrisson⁵, Ikuru Iwata⁶,
Genoveva Micheva⁷, Ken Mawatari⁸, Takuya Hashimoto^{1,2,6,9} and Mariko Kubo⁶

¹Waseda Research Institute for Science and Engineering, Faculty of Science and Engineering, Waseda University, 3-4-1, Okubo, Shinjuku, Tokyo 169-8555, Japan

²Department of Environmental Science and Technology, Faculty of Design Technology, Osaka Sangyo University, 3-1-1, Nakagaito, Daito, Osaka 574-8530, Japan

³Department of physics, School of Advanced Science and Engineering, Faculty of Science and Engineering, Waseda University, 3-4-1, Okubo, Shinjuku, Tokyo 169-8555, Japan

⁴Institute of Space and Astronautical Science, Japan Aerospace Exploration Agency, 3-1-1, Yoshinodai, Chuo-ku, Sagami-hara, Kanagawa 252-5210, Japan

⁵Observational Astrophysics, Department of Physics and Astronomy, Uppsala University, Box 516, SE-751 20 Uppsala, Sweden

⁶National Astronomical Observatory of Japan, 2-21-1 Osawa, Mitaka, Tokyo 181-8588, Japan

⁷Leibniz-Institut für Astrophysik, An der Sternwarte 16, D-14482 Potsdam, Germany

⁸Institute for Cosmic Ray Research, The University of Tokyo, 5-1-5 Kashiwa-no-Ha, Kashiwa, Chiba 277-8582, Japan

⁹Tomonaga Center for the History of the Universe (TCHoU), Faculty of Pure and Applied Sciences, University of Tsukuba, Tsukuba, Ibaraki 305-8571, Japan

Accepted 2020 August 14. Received 2020 August 13; in original form 2020 February 20

ABSTRACT

Using a sample of galaxies at $z \approx 3$ with detected Lyman Continuum (LyC) leakage in the SSA22 field, we attempt to verify a proposed indirect method for identifying cases with high LyC escape fraction f_{esc} based on measurements of the H β equivalent width (EW) and the β slope of the UV continuum. To this end, we present Keck/MOSFIRE H β emission line flux measurements of LyC galaxies (LCGs) at spectroscopic redshifts $z_{\text{spec}} \sim 3.3$, Lyman break galaxies (LBGs) at photometric redshifts $z_{\text{phot}} = 2.7\text{--}3.7$, and Ly α emitters at $z_{\text{phot}} = 3.1$. We also reconfirm the spectroscopic redshifts and measure the H β emission-line fluxes from two LCGs and six LBGs. For the LCG in our sample with the most extreme f_{esc} , as revealed by the direct detection of LyC photons, we find that the EW(H β)– β method gives a broadly consistent estimate for f_{esc} , although the error bars remain very large. We also discuss how a combination of f_{esc} measurements based on direct and indirect methods can shed light on the LyC escape mechanism and the anisotropy of the leakage.

Key words: galaxies: high-redshift – galaxies: ISM – galaxies: starburst.

1 INTRODUCTION

Cosmic reionization is a phase transition from the neutral to ionized state of the intergalactic medium (IGM), likely driven by ionizing radiation from star-forming galaxies (SFGs) and/or active galactic nuclei (AGNs; e.g. Madau, Haardt & Rees 1999; Madau & Haardt 2015; Robertson et al. 2015). Various observations indicate that the reionization process was completed by $z \sim 6$: the Gunn–Peterson optical depth (e.g. Fan et al. 2002, 2006), the clustering of Ly α emitters (LAEs; e.g. Ouchi et al. 2010, 2018), the evolution of the luminosity function of LAEs (e.g. Kashikawa et al. 2006, 2011; Itoh et al. 2018; Konno et al. 2018), the fraction of Ly α emitting galaxies in SFGs (e.g. Ono et al. 2012; Schenker et al. 2012), the Ly α damping wing in gamma-ray burst after-glow spectra (e.g. Totani et al. 2006, 2016; Greiner et al. 2009), and the kinetic Sunyaev–Zeldovich effect (e.g. Zahn et al. 2012; Planck Collaboration XLVII 2016). However, despite a great deal of effort to understand cosmic reionization, the detailed history, sources, and topology of this epoch are not yet understood.

In order to understand the dominant sources of cosmic reionization, the fraction of ionizing photons (Lyman continuum, hereafter LyC, at $\lambda_{\text{rest}} < 912\text{\AA}$) that escapes from SFGs/AGNs into the surrounding IGM, f_{esc} , is one of the most important physical quantities. For reionization by SFGs, a LyC escape fraction on the order of 10 per cent seems to be required (e.g. Inoue, Iwata & Deharveng 2006; Finkelstein et al. 2015, 2019; Bouwens et al. 2016). Based on current constraints, the contribution from AGNs to the reionization process moreover appears to be subdominant compared to that of SFGs (e.g. Micheva, Iwata & Inoue 2017a; Matsuoka et al. 2018; Kulkarni, Worseck & Hennawi 2019).

The simplest and most robust way to constrain f_{esc} is direct imaging and/or direct spectroscopic observations of the escaping LyC photons. The standard procedure is to estimate f_{esc} of SFGs/AGNs from their observed luminosity ratio of ionizing to non-ionizing ultraviolet (UV) radiation, $L_{\text{UV, obs}}/L_{\text{LyC, obs}}$, using assumptions on the intrinsic luminosity ratio of $L_{\text{UV, int}}/L_{\text{LyC, int}}$, the IGM absorption along its sightline, and the dust attenuation (e.g. Steidel, Pettini & Adelberger 2001; Inoue et al. 2005; Siana et al. 2007).

Since it is next to impossible to directly observe the LyC photons escaping from SFGs/AGNs at $z > 5$ due to foreground IGM absorption (Inoue & Iwata 2008), the LyC observations for lower- z

* E-mail: syamanaka@aoni.waseda.jp

analogues are important for inferring the likely f_{esc} of SFGs/AGNs in the epoch of cosmic reionization, and to test indirect methods of estimating f_{esc} .

Numerous attempts have been made to estimate the LyC escape fractions of individual SFGs at $z < 4$. Since Earth's atmosphere is very efficient in absorbing far-UV radiation, space telescopes such as the Far Ultraviolet Spectroscopic Explorer (*FUSE*) and the *Hubble Space Telescope* (*HST*) have very been important for studying the f_{esc} of local and/or low- z SFGs. Several detections of direct LyC radiation from $z < 1$ starburst galaxies have been made, typically with $f_{\text{esc}} \lesssim 10$ per cent (e.g. Bergvall et al. 2006; Leitert et al. 2011, 2013; Borthakur et al. 2014; Izotov et al. 2016a, b), although some objects have been reported with $f_{\text{esc}} \sim 40$ –70 per cent (Izotov et al. 2018a, b). At $z \approx 2$ –4, the f_{esc} values of SFGs have been investigated by both space and ground-based telescopes. In this redshift range, many individual objects appear to show relatively high f_{esc} ($f_{\text{esc}} \gtrsim 10$ per cent) compared to the local value (e.g. Steidel et al. 2001, 2018; Iwata et al. 2009, 2019; Mostardi et al. 2015; Shapley et al. 2016; Vanzella et al. 2016, 2018; Bian et al. 2017; Micheva et al. 2017b; Naidu et al. 2017; Fletcher et al. 2019).

At the same time, attempts to estimate the typical f_{esc} using stacked samples at $z = 1$ –3 indicate that this value may be much lower. These stacking analyses often result in non-detections of LyC, with corresponding upper limits at $f_{\text{esc}} < \text{several per cent}$ (e.g. Siana et al. 2007, 2010; Vanzella et al. 2010b; Grazian et al. 2016; Micheva et al. 2017b). A very low typical $f_{\text{esc}} \approx 0.5$ per cent has also been derived from the study of gamma-ray bursts at $z \approx 1.6$ –6.7 (Tanvir et al. 2019). Hence, the average f_{esc} at these intermediate redshifts may be on the low side of what would be required for cosmic reionization (but see Finkelstein et al. 2019 for an attempt to explain reionization with $f_{\text{esc}} \leq 5$ per cent). Whether the average f_{esc} increases as one approaches the epoch of reionization ($z > 6$) remains an open question.

Since studies of individual objects with LyC detections report significant f_{esc} values (from several per cent at $z \sim 0$ to 10–60 per cent at $z \sim 3$ –4), it is likely that the LyC escape depends strongly on physical quantities such as the properties of gas and dust in the ISM, the viewing angle, the star formation rate, and/or the stellar mass (e.g. Nestor et al. 2011, 2013; Mostardi et al. 2013). For a statistical discussion, it is important to collect data on LyC-detected SFGs that cover a wide parameter space in terms of physical characteristics. In numerical simulations, less-massive and/or UV fainter SFGs, which are more abundant than massive and/or UV brighter SFGs, are for instance often predicted to have high f_{esc} and hence contribute significantly to cosmic reionization (e.g. Yajima, Choi & Nagamine 2011; Wise et al. 2014; Paardekooper, Khochfar & Dalla Vecchia 2015).

Depending on the physical mechanism behind the leakage, this can have number of distinct effects on various spectral features. When the escape path is optically thin to Ly α photons ($\tau_{\text{Ly}\alpha} \sim 1$ for $\log N_{\text{H I}} \sim 13$), the escape path is also optically thin to LyC photons ($\tau_{\text{LyC}} \sim 1$ for $\log N_{\text{H I}} \sim 17$). Hence, one expects a positive correlation between f_{esc} and the emission-line EW of Ly α (e.g. Micheva et al. 2017b; Steidel et al. 2018). When assuming the link of the escape path between LyC and Ly α , the line profile of Ly α also becomes a probe for f_{esc} (Verhamme et al. 2015, 2017; Dijkstra, Gronke & Venkatesan 2016). The luminosity ratio of [O III] $\lambda\lambda$ 4959, 5007 and [O II] λ 3727, [O III]/[O II], has also been suggested as a probe for high- f_{esc} SFGs (Nakajima et al. 2013; Nakajima & Ouchi 2014). Indeed, very high f_{esc} ($f_{\text{esc}} \gtrsim 50$ per cent) are found among SFGs with high [O III]/[O II] at both low and high z (de Barros et al. 2016; Vanzella et al. 2016, 2018; Izotov et al. 2018a). Even so, Nakajima et al. (2019) report that no LyC escape is detected for some SFGs despite a high

[O III]/[O II] ratio. Hence, it seems that a high [O III]/[O II] ratio may be a necessary, rather than sufficient condition for LyC leakage.

Although there have been attempts to determine f_{esc} for SFGs at $z < 4$ from direct LyC measurements, our knowledge of f_{esc} is still far from complete. There are essentially five difficulties in estimating f_{esc} from direct LyC measurements. First of all, it is hard to directly observe the escaping LyC photons from high- z SFGs (and almost impossible from SFGs at $z > 5$) due to the foreground absorption by H I clouds in the IGM such as Lyman limit systems (e.g. Inoue & Iwata 2008; Inoue et al. 2014). Secondly, significant sightline-to-sightline variations in IGM absorption are predicted (Inoue & Iwata 2008; Vasei et al. 2016; Steidel et al. 2018), which may be difficult to assess for individual targets. In fact, Rivera-Thorsen et al. (2019) report on large variations among the multiply-imaged LyC spots from a gravitationally lensed SFG at $z = 2.4$. Thirdly, it is possible that the observed flux, which is assumed to be due to escaping LyC photons, does not come from SFGs at high z but from the foreground (low- z) interlopers (Vanzella et al. 2010a; Siana et al. 2015). Fourthly, the leakage may be anisotropic, so that the f_{esc} measured in our direction may deviate significantly from the total f_{esc} of the target galaxy. Finally, because the UV light especially at $\lambda_{\text{obs}} \lesssim 3000$ Å is absorbed by the Earth's atmosphere, we need space telescopes for the direct LyC measurements of low- z objects. In order to investigate the redshift evolution of f_{esc} and the detailed correlations between f_{esc} and other physical quantities, we would greatly benefit from an indirect method which can avoid these problems.

Zackrisson, Inoue & Jensen (2013) have proposed a scheme to indirectly assess f_{esc} from two observational quantities not affected by IGM attenuation – the H β line equivalent width (EW) and the rest-frame intrinsic UV spectral slope β , defined as $f_{\lambda} \propto \lambda^{\beta}$ at $\lambda_{\text{rest}} \sim 1300$ –2500 Å (Calzetti, Kinney & Storchi-Bergmann 1994). This EW(H β)– β method is based on the simple idea that a high fraction of LyC photons absorbed in H II regions of SFGs should result in stronger nebular emission and a larger EW(H β). The EW of nebular emission also depends on the production rate of LyC photons, but the UV spectral slope β can potentially be used to gauge this, as a blue UV slope is expected to go hand in hand with a high production rate. As a consequence, the distribution of SFGs across the EW(H β)– β diagram could make it possible to single out high- f_{esc} cases.

This method was designed for identifying extreme cases of LyC leakage in the $z > 6$ galaxy population, which are out of reach of direct LyC detection methods, and originally based on simple toy models for such galaxies. However, Zackrisson et al. (2017) also show the validity of this idea for SFGs at $z > 6$ in cosmological simulations. If verified, this could be a useful tool for studying LyC leakage with the *James Webb Space Telescope* (*JWST*), which will be able to spectroscopically detect H β in large samples of galaxies up to $z \approx 9$.

However, before attempting to apply the EW(H β)– β method to SFGs at $z > 6$, it would be very useful to verify this method with SFGs for which the LyC has been measured through direct means, so that the f_{esc} derived from the direct and indirect methods can be compared. This requires applying the method to galaxies at $z < 4$ and comes with a number of challenges. Observations have revealed that there is a trend in β with redshift in the sense that reionization-epoch galaxies tend to have bluer UV slopes (Bouwens et al. 2014), likely due to evolution in both dust attenuation and stellar population age (Wilkins et al. 2013). Without recalibrating the method to simulations at $z < 6$, it is therefore necessary to identify a suitable lower-redshift analogue with properties that match the $z > 6$ galaxy population as closely as possible. The ideal case would be to detect high levels of LyC from a galaxy with a very blue UV slope, indicative of

low dust reddening, although the exact β limit for this depends on $\text{EW}(\text{H}\beta)$ as well. The comparison may also be compromised due to the way anisotropic leakage, and uncertainties in the IGM line-of-sight absorption may affect the direct f_{esc} measurement. Despite these difficulties, we here set out to attempt this test, starting from a sample of $z \approx 3$ galaxies in the SSA22 field¹ where a prominent density peak of LBGs, LAEs, Ly α blobs and sub-mm galaxies at $z = 3.09$ have been reported (Steidel et al. 1998, 2000; Hayashino et al. 2004; Matsuda et al. 2004; Tamura et al. 2009; Yamada et al. 2012a; Umehata et al. 2014; Kubo et al. 2015).

In this paper, we present results of our K -band spectroscopic measurements of the $\text{H}\beta$ emission-line flux from Lyman Continuum Galaxies (hereafter LCGs), which are SFGs with direct LyC detections at $z \sim 3.3$, as well as Lyman break galaxies (LBGs) and LAEs in the SSA22 field. In the end, we are able to identify one very blue LCG for which the $\text{EW}(\text{H}\beta)$ – β method may be applied without modifications, and find that the f_{esc} estimated from this technique is broadly consistent with f_{esc} derived from the direct LyC measurement. Stronger constraints (and hence a more decisive test) would, however, require a significant reduction of the observational errors on both $\text{EW}(\text{H}\beta)$ and β .

In Section 2, we describe the details of our sample of LCGs/LBGs/LAEs. In Section 3, we describe the spectroscopic observations and the data reductions. In Section 4, we explain the method used for measuring the UV spectral slope β , the emission line flux, and $\text{EW}(\text{H}\beta)$. In Section 5, we show our main result, i.e. the $\text{EW}(\text{H}\beta)$ – β diagram. In Section 6, we discuss the $\text{EW}(\text{H}\beta)$ – β method in comparison to the direct LyC measurement. Our results are summarized in Section 7. In regard to the cosmological parameters, we assume $\Omega_{\text{m},0} = 0.3$, $\Omega_{\Lambda,0} = 0.7$, $H_0 = 70 \text{ km s}^{-1} \text{ Mpc}^{-1}$. Throughout this work, we adopt the AB magnitude system (Oke & Gunn 1983; Fukugita et al. 1996).

2 SAMPLE

2.1 Photometric catalogue

In this work, we use the SSA22 H I Tomography (SSA22HIT) master catalogue (Mawatari et al. in preparation). The purpose of the SSA22HIT project is to reveal the spatial distribution of H I gas in the SSA22 proto-cluster field through the use of Ly α forest tomography (Lee et al. 2014, 2018). For this purpose, they compile the photometry of available broad-band and narrow-band filters in the SSA22 field, and make a catalogue of LAEs and LBGs in a range of photometric redshift ($z_{\text{phot}} = 2.7\text{--}3.7$). The catalogue includes the photometry of broad-band and narrow-band filters of the Canada-France-Hawaii Telescope (CFHT)/MegaCam (Boulade et al. 2003), Subaru/Suprime-Cam (Scam; Miyazaki et al. 2002), Subaru/Hyper Suprime-Cam (HSC; Miyazaki et al. 2012, 2018), Subaru/MOIRCS (Suzuki et al. 2003; Ichikawa et al. 2006), UKIRT/WFCAM (Casali et al. 2007), and *Spitzer*/IRAC (Fazio et al. 2004). The source detection on the Subaru/Scam i' -band image (Nakamura et al. 2011) and multi-band photometry are performed by using SEXTRACTOR² version 2.5.0 (Bertin & Arnouts 1996). Except for the *Spitzer* data, the point spread function (PSF)-matched images are created by convolving the original images with Gaussian kernels to match a PSF with full width at half-maximum (FWHM) = 1.1 arcsec. The

PSF FWHM of 1.1 arcsec is adopted because the PSF FWHM of Subaru/ R band is ~ 1.1 arcsec, which is larger than that of the other filters except for the *Spitzer* data. The 2.2 arcsec-diameter ($= 2 \times \text{PSF}$) aperture flux is measured for the PSF-matched images.

In our analysis, we use the photometry measured for the PSF-matched images of Subaru/Scam R (Hayashino et al. 2004), Subaru/Scam i' and z' (Nakamura et al. 2011), Subaru/Scam NB359 (Iwata et al. 2009), Subaru/HSC y (HSC Subaru Strategic Program Public Data Release 1; Aihara et al. 2018), and UKIRT/WFCAM K (UKIRT Infrared Deep Sky Survey Data Release 10; Lawrence et al. 2007). The Subaru/NB359 is a unique narrow-band filter that directly traces LyC photons from galaxies at $z \gtrsim 3.06$ (Iwata et al. 2009; Micheva et al. 2017b). The central wavelength, the FWHM, and the transmittance larger than 10 per cent are 359 nm, 15 nm, and [350 nm, 371 nm], respectively. We list the detail of the imaging data used in this work in Table 1.

2.2 Spectroscopic targets

Our spectroscopic sample consists of 42 galaxies in the SSA22 field. Two of them are LCGs at spectroscopic redshifts ($z_{\text{spec}} \sim 3.3$) and the main targets for our MOSFIRE observation. They are selected from a sample of the LyC sources reported by Iwata et al. (2009) and Micheva et al. (2017b). In this paper, we will refer to them as LCG-1 and LCG-2. In order to observe these main targets, we set two mask fields, Mask-1 and Mask-2. 37 objects are complementary LBGs at $z_{\text{phot}} \sim 3.2 \pm 0.3$, which are selected from the SSA22HIT master catalogue. We will refer to these as SSA22-LBGs in this paper. The remaining three objects are LAEs at $z_{\text{phot}} = 3.1$ (Yamada et al. 2012a, b) which are observed as filler objects (hereafter Y12LAEs). Y12LAE-2 and Y12LAE-3 are taken from the LAE candidates studied in Yamada et al. (2012a) that show significant narrow-band excess but below their criteria for the robust LAE sample. Our sample is summarized in Table 2. The details are described in the following.

2.2.1 LCG-1 and LCG-2

LCG-1 is reported by Micheva et al. (2017b) as ‘LBG03’ in their paper. In the LyC image (Subaru/NB359 filter), two small LyC clumps are observed, separated by $\Delta r \sim 0.8$ arcsec (see fig. 2 in Micheva et al. 2017b) from the peak of the rest-frame UV continuum (Subaru/ R filter). We set the MOSFIRE slitlet on the peak of the UV continuum and use the wider slit width due to the complex morphology of LyC and UV continuum. The spectroscopic redshift is $z_{\text{spec, Ly}\alpha} = 3.287$ which is measured from the optical low-resolution spectroscopy for the Ly α emission line (Micheva et al. 2017b). Due to the blue NB359 – R colour, we consider LCG-1 to be the primary high- f_{esc} candidate in our sample.

LCG-2 is also reported by Micheva et al. (2017b) as ‘LBG04’ in their paper. The LyC image reveals a single small LyC clump, with a spatial offset of $\Delta r \sim 0.8$ arcsec from the peak of the rest-frame UV continuum (see fig. 2 in Micheva et al. 2017b). In this case, we set the slitlet to simultaneously cover the peak of the UV continuum and the LyC clump. The spectroscopic redshift is measured by Steidel et al. (2003). In Steidel et al. (2003), LCG-2 is referred to as ‘SSA22b-oD8’ and shows $z_{\text{spec, Ly}\alpha} = 3.323$ and $z_{\text{spec, abs}} = 3.311$. According to Steidel et al. (2003), $z_{\text{spec, Ly}\alpha}$, and $z_{\text{spec, abs}}$ are measured from the Ly α emission line and the average of some absorption lines, respectively. Due to the red NB359 – R colour, we consider LCG-2 to be the low- f_{esc} candidate of our sample.

¹ SSA22 stands for Small Selected Area at R.A. 22h (Cowie et al. 1988; Lilly, Cowie & Gardner 1991).

² <http://www.astromatic.net/software/sextractor>

Table 1. Summary of a part of the imaging data compiled by Mawatari et al. in preparation.

Instrument	Filter	PSF FWHM	Limiting mag.	$\lambda_{\text{rest, eff}}$	Reference
		(original, arcsec)	(smoothed, 2.2 arcsec ϕ , 5 σ)	(if $z_{\text{source}} = 3.3$)	
Subaru/Scam	<i>R</i>	1.08	26.5	1520	Hayashino et al. (2004)
	<i>i'</i>	0.76	26.3	1790	Nakamura et al. (2011)
	<i>z'</i>	0.76	25.6	2110	Nakamura et al. (2011)
	<i>NB359</i>	0.84	26.1	830	Iwata et al. (2009)
Subaru/HSC	<i>y</i>	0.56	24.1	2270	Aihara et al. (2018)
UKIRT/WFCAM	<i>K</i>	0.86	22.9	5150	Lawrence et al. (2007)

Note. We only list the broad-band and narrow-band filters used for our analysis, i.e. the estimation of UV spectral Slope β and the measurements of EW of H β .

2.2.2 SSA22-LBGs and Y12LAEs

The SSA22-LBGs, selected from the SSA22HIT master catalogue, all have $i' < 26.4$ ($S/N > 5$) at $z_{\text{phot}} = 2.7\text{--}3.7$. We set the slitlets on the peak of the UV continuum (Subaru/*i'* filter) for each object. The SSA22-LBGs satisfy either the colour–colour selection (i.e. classical Lyman break technique) or the photometric redshift estimated by using Hyperz (Bolzonella, Miralles & Pelló 2000), or both. For our MOSFIRE observation, we first choose the SSA22-LBGs with blue UV spectral slopes β ($\beta < -2.0$) as the high-priority targets from the catalog. After that, we fix the two mask fields so as to maximize the number of high-priority targets. The remaining slitlets are set to other SSA22-LBGs. There is still a margin of slitlets which is used for the three Y12LAEs. Under the SSA22HIT project, some of the SSA22-LBGs are observed with the Deep Imaging Multi-Object Spectrograph (DEIMOS; Faber et al. 2003) mounted on the Keck-II telescope. In cases where the spectroscopic redshift has been successfully measured by the SSA22HIT project, we show the z_{spec} value in Table 2.

There are some SSA22-LBGs significantly detected in the LyC image in our sample: 11 objects display a LyC detection at the 3σ level ($NB359 < 26.7$). 6 out of the 11 objects also exhibit a blue UV slope β ($\beta < -2.0$), whereas the remaining 5 objects exhibit a red UV slope β ($\beta > -2.0$). Initially, we considered them as possible LCG candidates. However, from our MOSFIRE observations, we cannot identify any emission lines in any of these targets. Therefore, we conclude that these LBGs are not $z \sim 3$ galaxies and that the $NB359$ flux is not LyC. Hence, we do not use these object in the following analysis.

2.3 Rough estimation of LyC escape fraction

Fig. 1 shows an observed colour–magnitude diagram that indicates a rough f_{esc} value and UV flux for our LCGs/SSA22-LBGs. Since the Subaru/ $NB359$ directly traces LyC photons from galaxies at $z \gtrsim 3.06$, the vertical axis represents the observed flux density ratio $f_{\nu, \text{UV}}/f_{\nu, \text{LyC}}$. The horizontal magenta line indicates $f_{\text{esc}} = 0.5$ assuming a set of standard parameters: IGM transmission $T_{\text{IGM}} = 0.4$ (Inoue et al. 2014), UV dust attenuation $A_{\text{UV}} = 1.67$ (Micheva et al. 2017b), and the intrinsic LyC-to-UV luminosity ratio $L_{\text{UV}}/L_{\text{LyC}} = 3$, where L is in units of $\text{erg s}^{-1} \text{Hz}^{-1}$ (e.g. Steidel et al. 2001; Inoue et al. 2005). In general, the T_{IGM} , A_{UV} , and $L_{\text{UV}}/L_{\text{LyC}}$ values change from galaxy to galaxy. For example, the $L_{\text{UV}}/L_{\text{LyC}}$ value ranges from 1.5 to 5.5 depending on the stellar population age (0 Myr–1 Gyr) and the metallicity ($0.05 Z_{\odot}\text{--}Z_{\odot}$) in the case of constant star formation history (SFH) and Salpeter (1955) initial mass function (IMF) with $[0.1 M_{\odot}\text{--}100 M_{\odot}]$ (Inoue et al. 2005). As a result, the observed colour of $NB359 - R$ for $f_{\text{esc}} = 0.5$ (magenta line in Fig. 1) changes from

0.5 to 1.9; the plausible f_{esc} value of LCG-1 changes to >0.5 . The assumed parameter, $L_{\text{UV}}/L_{\text{LyC}} = 3$, means the relatively younger age (a few $\times 10$ Myr) and the lower metallicity ($Z < Z_{\odot}$), which is preferable to LCG-1 due to its blue $NB359 - R$ colour. These parameters (T_{IGM} , A_{UV} , and $L_{\text{UV}}/L_{\text{LyC}}$) should be carefully estimated by the spectral energy distribution (SED) fitting analysis for each object (e.g. Fletcher et al. 2019). In this paper, the rough f_{esc} estimate provided by this figure will be used in an attempt to test the EW(H β)– β method. However, we intend to carry out a more careful f_{esc} estimation for each object in future works by using a z_{spec} catalog for the SSA22HIT project.

As indicated by Fig. 1, LCG-1 appears to have $f_{\text{esc}} \gtrsim 0.5$, whereas LCG-2 and other SSA22-LBGs for which z_{spec} is confirmed by our MOSFIRE observation (green circles overplotted on grey crosses) appear to have $f_{\text{esc}} < 0.5$. The one exception is SSA22-LBG-08 ($NB359 - R \sim 1.1$). While this objects seems to have $f_{\text{esc}} \sim 0.5$, the Subaru/ $NB359$ filter is contaminated by another object close to the SSA22-LBG-08. Therefore, we adopt $f_{\text{esc}} < 0.5$ for SSA22-LBG-08 as well. We note two of the green circles are almost overlapped due to the same R -band magnitude and the non-detection of $NB359$, although there are ten z_{spec} -confirmed SSA22-LBGs in Fig. 1. Some of the other SSA22-LBGs (grey crosses only) also show the significant detection with $NB359$ and a high f_{esc} value. However, we are unable to confirm z_{spec} of the $NB359$ -detected SSA22-LBGs due to either a single or no emission line in our MOSFIRE observation. It is therefore likely that the Subaru/ $NB359$ filter does not trace the LyC emission for these objects and we will not discuss these objects further.

3 MOSFIRE OBSERVATIONS

3.1 Observation and data reduction

We conduct K -band multiobject spectroscopy with the Multi-Object Spectrometer For Infra-Red Exploration (MOSFIRE; McLean et al. 2010, 2012) on the Keck-I telescope. The purpose of these observations is to determine the spectroscopic redshift using strong emission lines such as [O III] $\lambda\lambda$ 4959, 5007, and to measure the H β emission-line flux. The data were obtained on 2016 August 27 during photometric conditions with seeing 0.4–0.6 arcsec. We applied the ABA B' dithering pattern with a nod amplitude of 3.0 arcsec (A–B) and 2.4 arcsec (A'–B'). We mainly used slit widths of 0.7 arcsec, which corresponds to a spectral resolution $R \sim 3600$ in the K band, although a slit width of 0.8 arcsec was used for LCG-1 to cover the LyC emitting regions (see Section 2.2.1).

We use two slit masks, Mask-1 and Mask-2, for our 42 LCGs/LBGs/LAEs. The field of view covered by the two slit-

Table 2. Summary of the Mask-1 and Mask-2 samples.

Name	RA	Dec.	z_{spec}^a	NB359 ^b	R ^b	K ^b	Reference ^c
Mask-1							
LCG-1 ^d	22:17:08.12	00:09:58.08	3.287	25.18	24.69	23.46	(1), (2)
SSA22-LBG-01	22:17:13.56	00:07:28.93	3.087	99.00	25.17	24.19	(3)
SSA22-LBG-02	22:17:06.26	00:07:39.03		99.00	25.39	99.00	(3)
SSA22-LBG-03	22:17:09.93	00:06:02.30		99.00	25.49	24.27	(3)
SSA22-LBG-04	22:17:10.55	00:05:01.51		25.71	24.99	99.00	(3)
SSA22-LBG-05	22:17:04.73	00:06:20.91	3.112	99.00	25.59	24.55	(3)
SSA22-LBG-06	22:17:04.96	00:06:08.30		99.00	25.31	99.00	(3)
SSA22-LBG-07	22:17:04.38	00:09:20.13		24.70	24.49	23.79	(3)
SSA22-LBG-08	22:17:07.97	00:05:04.96		26.51	25.40	24.18	(3)
SSA22-LBG-09	22:17:15.33	00:04:44.39		26.96	24.88	99.00	(3)
SSA22-LBG-10	22:17:13.39	00:07:52.39		99.00	25.10	23.61	(3)
SSA22-LBG-11	22:17:09.94	00:07:19.94		99.00	25.29	24.14	(3)
SSA22-LBG-12	22:17:13.60	00:06:40.05		27.02	24.42	23.56	(3)
SSA22-LBG-13	22:17:08.65	00:06:03.99	2.869	26.51	24.87	23.92	(3)
SSA22-LBG-14	22:17:08.29	00:04:20.93		26.74	25.61	24.43	(3)
SSA22-LBG-15	22:17:13.07	00:05:46.04		99.00	25.10	99.00	(3)
SSA22-LBG-16	22:17:12.56	00:08:52.28		99.00	25.47	99.00	(3)
SSA22-LBG-17	22:17:02.60	00:08:26.93		99.00	25.10	24.17	(3)
SSA22-LBG-18	22:17:10.27	00:04:40.23		26.85	25.05	24.13	(3)
SSA22-LBG-19	22:17:04.88	00:07:51.98		27.13	25.33	99.00	(3)
Y12LAE-1 ^e	22:17:01.58	00:08:36.71		–	–	–	(4)
Y12LAE-2 ^e	22:17:03.59	00:07:09.87		–	–	–	(4)
Mask-2							
LCG-2 ^d	22:17:23.55	00:03:57.61	3.311	26.64	23.44	22.54	(1), (2)
SSA22-LBG-09	22:17:15.33	00:04:44.39		26.96	24.88	99.00	(3)
SSA22-LBG-12	22:17:13.60	00:06:40.05		27.02	24.42	23.56	(3)
SSA22-LBG-20	22:17:34.30	00:03:48.72		24.21	23.96	24.07	(3)
SSA22-LBG-21	22:17:21.76	00:05:58.43		26.30	25.17	24.11	(3)
SSA22-LBG-22	22:17:16.07	00:04:32.75		27.42	25.50	24.34	(3)
SSA22-LBG-23	22:17:29.97	00:05:10.33		27.05	25.22	24.26	(3)
SSA22-LBG-24	22:17:27.76	00:05:27.47		99.00	25.72	23.77	(3)
SSA22-LBG-25	22:17:31.10	00:06:18.31		26.85	26.03	99.00	(3)
SSA22-LBG-26	22:17:26.56	00:04:13.81		27.08	24.50	24.45	(3)
SSA22-LBG-27	22:17:25.13	00:06:14.46		99.00	25.77	99.00	(3)
SSA22-LBG-28	22:17:17.72	00:05:45.27		26.67	25.33	99.00	(3)
SSA22-LBG-29	22:17:32.95	00:04:11.91		99.00	25.14	23.16	(3)
SSA22-LBG-30	22:17:28.34	00:04:45.57		99.00	24.97	24.59	(3)
SSA22-LBG-31	22:17:14.44	00:05:00.02		26.68	24.66	23.30	(3)
SSA22-LBG-32	22:17:22.68	00:06:10.35	3.906	26.47	25.19	99.00	(3)
SSA22-LBG-33	22:17:12.47	00:06:37.72		99.00	25.13	99.00	(3)
SSA22-LBG-34	22:17:25.80	00:05:48.64		99.00	25.08	23.36	(3)
SSA22-LBG-35	22:17:18.00	00:04:09.03		99.00	25.41	99.00	(3)
SSA22-LBG-36	22:17:20.01	00:05:42.18		26.03	25.32	23.95	(3)
SSA22-LBG-37	22:17:31.91	00:04:16.57		26.09	25.06	24.10	(3)
Y12LAE-3	22:17:31.75	00:06:17.66		99.00	26.00	99.00	(4)

^aWhen the spectroscopic redshift has been confirmed by the previous works, we show the values.^bThe entry 99.00 indicates a non-detection at the 1σ level.^c(1) Iwata et al. (2009); (2) Micheva et al. (2017b); (3) Mawatari et al. in preparation; (4) Yamada et al. (2012a, b).^dThe NB359 and R-band magnitudes are same as the total magnitude shown in Micheva et al. (2017b).^eNot listed in SSA22HIT master catalogue due to the non-detections in the Subaru/*i'*-band.

masks partially overlap, and SSA22-LBG-09 and SSA22-LBG-12 are observed using both slit masks. In addition to our LCGs/SSA22-LBGs targets, we also assign a slitlet on a bright and point-source like object ($K \sim 20$) in each slit mask to assess slit losses. The exposure time of Mask-1 and Mask-2 are 2.45 and 0.5 h, respectively. Due to the short exposure time used for Mask-2, we fail to detect emission lines from most of the targets observed in this setting. We only use LCG-2 and SSA22-LBG-22 from Mask-2 for our following analysis.

The data reduction is performed by using the MOSFIRE data reduction pipeline (DRP),³ which was developed by the MOSFIRE instrument team (Steidel et al. 2014). As a result, we obtain reduced 2D spectra that are flat-fielded, wavelength calibrated, rectified, and sky subtracted. In the wavelength calibration procedure, we search for the best solution for each slitlet from the combination of OH

³<https://keck-datareductionpipelines.github.io/MosfireDRP>

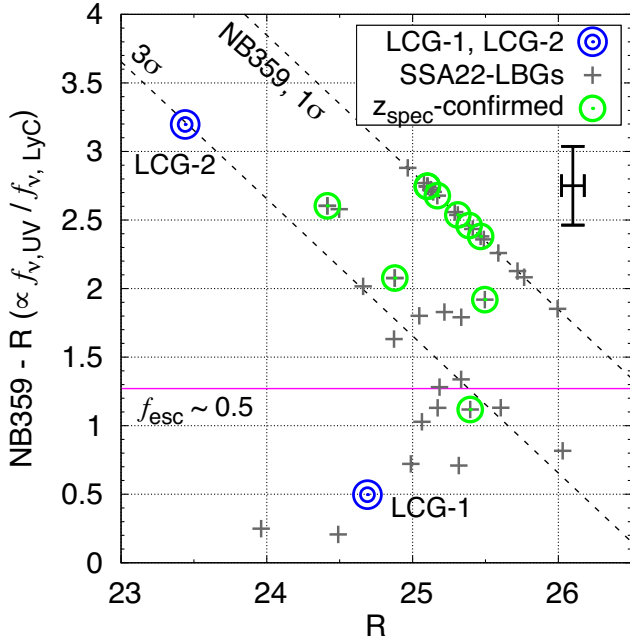


Figure 1. Observed colour-magnitude diagram of $NB359 - R$ versus R . The blue double circles show our main targets, LCG-1 and LCG-2. The grey crosses denote SSA22-LBGs. The green circles overlotted on the grey crosses mark the redshift-confirmed SSA22-LBGs, after MOSFIRE spectroscopy. The black error bars at top right indicate the average error of $NB359 - R$ and R . The horizontal magenta line indicates $f_{\text{esc}} \sim 0.5$ under the assumption of a set of standard parameters (see Section 2.3).

night sky lines and arc lines of a neon lamp. According to Steidel et al. (2014), the wavelength of the final 2D spectra are reduced to the vacuum wavelength and corrected for the heliocentric velocity. Therefore, we do not apply any additional correction to the reduced 2D spectra. The 1D spectra with their 1σ uncertainties are extracted from the reduced 2D spectra by using the BMPE⁴ software developed by the MOSFIRE Deep Evolution Field team (MOSDEF; Freeman et al. 2019). For the flux calibration, we use a telluric standard AOV star, HIP 80974, and the bright object in each slit mask. The telluric star is observed at similar airmass as the science frames. The total flux of the bright object is calculated from the UKIRT/K-band photometry after taking the filter response of the UKIRT/K-band into account. In the procedure for the flux calibration, the 1D spectra are simultaneously corrected for slit losses.

We show the reduced 2D and the extracted 1D spectra of LCG-1 in Fig. 2 as an example. In this case, we can easily identify some emission lines, and we can extract the 1D spectrum. In some cases, however, we are unable to identify any emission lines or the continuum from the 2D spectrum at the object position, and hence refrain from extracting a 1D spectrum. In Appendix, we summarize all the reduced 2D spectra and the successfully extracted 1D spectra.

3.2 Quick summary of MOSFIRE observations

3.2.1 LCG-1 and LCG-2

For LCG-1, we detect the three emission lines ([O III] $\lambda\lambda$ 4959, 5007 and H β), and then confirm its systemic spectroscopic redshift from

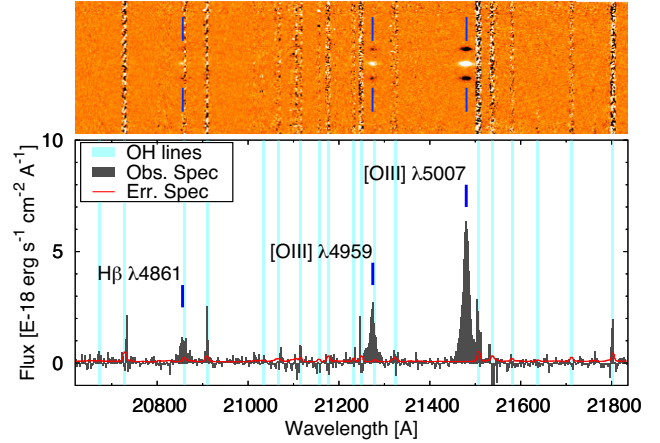


Figure 2. The reduced 2D (top) and the extracted 1D spectra (bottom) of LCG-1. In both panels, the identified emission lines are marked with blue thick lines. In the bottom panel, the filled dark grey histogram and the red lines represent the observed spectrum and the noise spectrum, respectively, in units of $10^{-18} \text{ erg s}^{-1} \text{ cm}^{-2} \text{ \AA}^{-1}$. The vertical cyan lines indicate the wavelengths of OH night sky lines.

[O III] λ 5007 to be $z_{\text{spec, sys}} = 3.2890$. This value is consistent with (or slightly larger than) that from the Ly α emission line inferred from optical low-resolution spectroscopy. Although the Ly α emission line may be blueshifted compared with its systemic redshift, we need the optical medium-/high-resolution spectroscopy to conclude the shift. As shown in Fig. 2, part of the H β emission line is affected by OH night sky lines. However, we judge their influence on the total line flux to be small because we are able to measure the peak of the H β emission line. Moreover, we do not find any other emission lines stemming from lower redshifts. Hence, there is no evidence that the LyC flux inferred for this target from the Subaru/NB359 image is contaminated by low- z interlopers.

For LCG-2, we detect the three emission lines ([O III] $\lambda\lambda$ 4959, 5007 and H β). The systemic redshift estimated from [O III] λ 5007 is $z_{\text{spec, sys}} = 3.3152$, which is consistent with the redshifts reported by Steidel et al. (2003) and Micheva et al. (2017b) since $z_{\text{spec, sys}}$ typically lies somewhere between $z_{\text{spec, Ly } \alpha}$ and $z_{\text{spec, abs}}$ (e.g. Steidel et al. 2010). Since we do not find any other suspicious emission lines, there is no evidence that the LyC photons detected in the Subaru/NB359 filter stems from a low- z interloper. The bright absolute UV magnitude of LCG-2 ($M_{\text{UV}} \sim -22.0$) could potentially indicate the existence of the faint AGN in this source. In fact, the observed line width of H β is relatively large ($\text{FWHM}_{\text{raw}} \sim 300 \text{ km s}^{-1}$; Table A1). However, we do not find any other features of AGNs from our MOSFIRE observation. In order to conclude the existence of AGNs, we would need further follow-up observations such as optical spectra covering C IV λ 1549 and He II λ 1640.

3.2.2 SSA22-LBGs and Y12LAEs

For SSA22-LBGs and Y12LAEs, one to three emission lines are confirmed for some of the targets after visual inspection of the 2D images and the 1D spectrum. There exist six SSA22-LBGs for which we detected the three emission lines ([O III] $\lambda\lambda$ 4959, 5007 and H β). For five SSA22-LBGs/Y12LAEs, we confirmed their spectroscopic redshifts through the detection of two emission lines, although their H β total flux was not measured (for various reasons – see the next paragraph). For the rest 29 SSA22-LBGs/Y12LAEs, we detected only a single or no emission line and could not identify their redshifts by our

⁴<https://github.com/billfreeman44/bmep>

Table 3. Summary of the observed values used for the EW(H β)- β method.

Name	z_{spec}^a	m_K^b	β^c	$F_{\text{H}\beta}^d$ ($10^{-18} \text{ erg s}^{-1} \text{ cm}^{-2}$)	EW _{rest} (H β) ^e (Å)	f_{esc}^f
Mask-1						
LCG-1	3.2890	23.46	-2.44 ± 0.34	19.82 ± 0.96	104.67 ± 74.53	≤ 0.7
SSA22-LBG-01	3.0892	24.19	-2.35 ± 0.45	11.72 ± 0.64	[38.83–232.07]	0.0
SSA22-LBG-02	3.3437	99.00	-2.10 ± 0.56	10.36 ± 0.68	[36.27–170.19]	0.0
SSA22-LBG-09	2.9768	99.00	-2.13 ± 0.32	13.75 ± 1.64	[38.68–163.09]	0.0
SSA22-LBG-10	3.2013	23.61	-1.78 ± 0.39	14.25 ± 0.61	55.71 ± 28.80	0.0
SSA22-LBG-12	3.1118	23.56	-2.25 ± 0.22	27.72 ± 1.31	175.65 ± 143.71	0.0
SSA22-LBG-16	3.1041	99.00	-1.72 ± 0.54	4.32 ± 0.58	[11.82–52.55]	0.0
Mask-2						
LCG-2	3.3152	22.54	-1.41 ± 0.04	53.86 ± 3.10	86.62 ± 19.62	≤ 0.5
SSA22-LBG-22	3.3490	24.34	-1.64 ± 0.57	< 2.19	< 22.33	

^a z_{spec} is estimated from the [O III] λ 5007 emission line.^b The magnitude observed with UKIRT/K band. The values are same as those listed in Table 2.^c The UV spectral slope β and its uncertainty.^d The symbol of $<$ indicates a 3σ upper limit.^e [XX–YY] indicates the permitted range of EW_{rest}(H β) (see Section 4.3).^f f_{esc} is inferred from the EW(H β)- β method.

observation itself. In the following analysis, we use all of six SSA22-LBGs with the detection of three emission lines and only one SSA22-LBG (SSA22-LBG-22) with the detection of two emission lines.

We here describe the details of the five objects with the detection of two emission lines to motivate the reason for using only SSA22-LBG-22 for our analysis. For SSA22-LBG-22, our observation significantly detects [O III] λ 5007, and marginally detects [O III] λ 4959 ($S/N \lesssim 5$) due to blending with OH night sky lines. It is in principle possible that the detection of [O III] λ 4959 is spurious and SSA22-LBG-22 is actually a lower- z object. However, the spectrum does not contain any further unidentified emission lines and the H β wavelength is not affected by the OH night sky lines. Therefore, we consider SSA22-LBG-22 as a robust member of the redshift-confirmed sample.

Three of the five objects are SSA22-LBG-06, 17, and Y12LAE-1. Their H β wavelengths are not covered by our observation due to the slitlet configuration. Because we cannot obtain any information about H β , we do not use these objects. The last of the five objects is SSA22-LBG-08, for which the region covering the expected H β wavelength is affected by OH sky lines. Due to the poor constraint on the H β emission, we refrain from using SSA22-LBG-08 in our analysis.

4 ANALYSIS

4.1 UV spectral slope

In this work, we measure the UV spectral slope β from the photometry of Subaru/ R -, i' -, z' -, and HSC/ y -band filters by using linear weighted least-squares fitting. According to Finkelstein et al. (2012) and Rogers, McLure & Dunlop (2013), we apply the following function to the observed photometry:

$$m(\lambda_x) = -2.5(\beta + 2) \log \lambda_x + \text{const}, \quad (1)$$

where λ_x is the effective wavelength of x th broad-band filter, $m(\lambda_x)$ is the measured magnitude of the x th broad-band filter, and ‘Const’ is a constant value. We adopt the best-fitting value of the fitting with equation (1) on all R -, i' -, z' -, and y -band magnitudes as the β value. The uncertainty on the fitting is also adopted as the uncertainty in the β value. Our sample consists of LBGs at $z \sim 3.2 \pm 0.3$ and LAEs at $z = 3.1$. At these redshifts, the applied broad-band filters of R -, i' -, z' -, and y

in the fitting are optimal for avoiding redshifted strong spectral features such as the Ly α break ($\lambda_{\text{rest}} \sim 1216 \text{ Å}$) or the Balmer break ($\lambda_{\text{rest}} \sim 3600 \text{ Å}$). Our β values and their uncertainties are listed in Table 3.

4.2 Emission-line measurement

We adopt a Monte Carlo method for measuring the line profile, the total flux, and the associated uncertainties for each emission line. We first perturb the 1D spectrum according to its 1σ noise spectrum at each pixel (hereafter referred to as a fake spectrum). We then identify the brightest emission line as [O III] λ 5007 from the fake spectrum, and estimate the spectroscopic redshift, z_{spec} , by fitting a single Gaussian profile to the line. If part of the emission line is strongly affected by the OH night sky lines, we mask the pixels in the fitting. The OH night sky lines are identified by using night sky line lists on the MOSFIRE official website.⁵ We adopt 6.0 Å as the width of each OH line assuming the spectral resolution $R \sim 3600$. We also calculate the total line flux by integrating the Gaussian profile. We repeat this procedure 10^4 times, and finally obtain the 10^4 measurements of the z_{spec} value, the FWHM of the line profile, and the total flux from the fake spectra. The mean and standard deviation of the distribution of the measurements are adopted as the best value and its uncertainty, respectively. By using the best z_{spec} value, we search for the redshifted emission lines of [O III] λ 4959 and H β from each of the 10^4 fake spectra. When we identify the emission lines, we fit a single Gaussian profile, whose centre is fixed based on the best z_{spec} value, to each line. In a similar way to [O III] λ 5007, we obtain the best FWHM value and the best total flux of [O III] λ 4959 and/or H β from the 10^4 fake spectra. For the line fitting, we adopt $\lambda_{\text{rest, vac}} = 5008.240, 4960.295, \text{ and } 4862.683 \text{ Å}$, which are obtained from the Atomic Line List version 2.04,⁶ as a vacuum wavelength of [O III] $\lambda\lambda$ 5007, 4959, and H β , respectively.

As for SSA22-LBG-22 (the object without the detection of H β), we measure the 3σ upper-limit of the H β emission line. On the basis of error propagation, we estimate a 1σ uncertainty in the H β emission-line flux from $\sqrt{\sum \sigma^2}$ where σ indicates the 1σ uncertainty per spectral element from the noise spectrum. For the

⁵ https://www2.keck.hawaii.edu/inst/mosfire/wavelength_calibration.html⁶ <http://www.pa.uky.edu/~peter/atomic/>

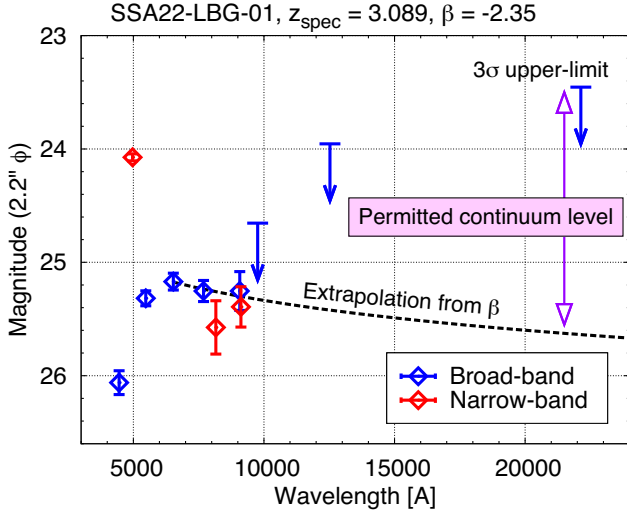


Figure 3. Illustration for estimating the permitted range of the continuum flux density. As an example, we show the spectral energy distribution of SSA22-LBG-01. The blue diamonds refer to broad-band photometry of B , V , R , i' , z' , y , J , and K from left to right. The red diamonds indicate narrow-band photometry of $NB497$, $NB816$, and $NB912$ from left to right. The black dashed line, which shows the best-fitting UV spectral slope β , is extrapolated to longer wavelengths. The purple double arrow indicates the permitted range of the continuum flux density for SSA22-LBG-01.

range of the summation, we adopt $\lambda = \lambda_{H\beta, \text{vac}}(1 + z_{\text{spec}}) \pm 3\sigma_{[\text{O III}]}$ where $\sigma_{[\text{O III}]}$ is the best standard deviation of $[\text{O III}] \lambda 5007$ calculated by $\sigma_{[\text{O III}]} = \text{FWHM}/(2\sqrt{2 \ln 2})$. In the estimation for the upper-limit, we assume that the FWHM of $H\beta$ is similar to that of $[\text{O III}] \lambda 5007$. We consider $\pm 3\sigma_{[\text{O III}]}$ to be optimal since a wider summation range results in an overestimation of the upper limit due to contamination of the OH night sky lines.

In Table 3, we show the $H\beta$ total flux for LCG-1, LCG-2, and SSA22-LBGs from which we measure the best total flux of $H\beta$. The detail results of the line measurements for our targets are described in Appendix A, and listed in Tables A1 and A2.

4.3 EW measurement

The EW of $H\beta$ is obtained by $\text{EW}(H\beta) = F_{H\beta}/f_{\lambda, \text{cont}}$, where $F_{H\beta}$ is the total flux of $H\beta$ and $f_{\lambda, \text{cont}}$ is the continuum flux density at the wavelength of $H\beta$ in units of $\text{erg s}^{-1} \text{cm}^{-2} \text{\AA}^{-1}$. While we obtain $F_{H\beta}$ through our MOSFIRE observations, there are no objects detected at a significant level ($> 3\sigma$) in UKIRT/ K among the SSA22-LBGs due to the short exposure time of K ($K_{3\sigma} \sim 23.5$). However, two SSA22-LBGs are detected at a 2σ level (SSA22-LBG-10 and SSA22-LBG-12). For LCG-1, LCG-2, and the two SSA22-LBGs, therefore, we estimate $f_{\lambda, \text{cont}}$ from the K -band photometry as an average continuum flux density around the wavelength of $H\beta$ after subtracting the contribution from the $[\text{O III}]$ and $H\beta$ emission lines to the filter. We simply estimate the uncertainty in $\text{EW}(H\beta)$ from the uncertainty in the $H\beta$ flux and the K -band magnitude on the basis of error propagation. The measured $\text{EW}(H\beta)$ are summarized in Table 3.

For other SSA22-LBGs, we regard them as the UKIRT/ K non-detection sample. We estimate the permitted range of the continuum flux density as follows. Fig. 3 illustrates our idea. The upper limit of the flux density is obtained from the 3σ limiting magnitude of the UKIRT/ K -band image after correcting for the contribution of the $[\text{O III}]$ and $H\beta$ emission lines to the filter. The lower limit of the flux

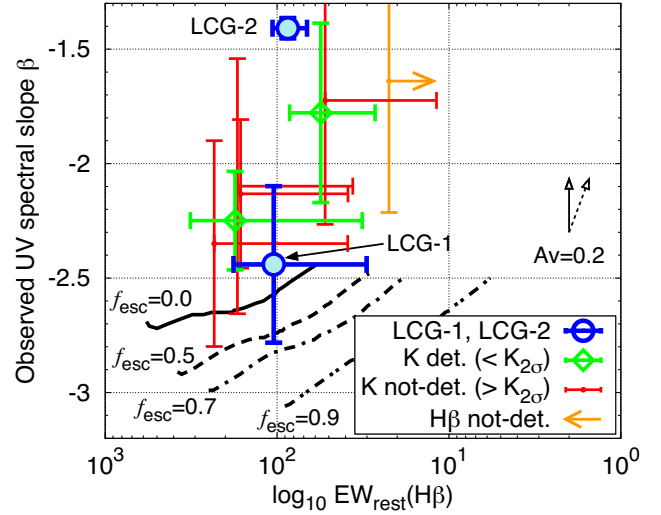


Figure 4. $\text{EW}(H\beta)$ – β diagram. The x-axis is reversed as the $\text{EW}(H\beta)$ value increases from right to left. The blue circles filled with cyan show our main targets, LCG-1 and LCG-2. The green diamonds show the SSA22-LBGs with marginal K -band detection at $> 2\sigma$ level (K -LBGs). The red error bars show the SSA22-LBGs that are undetected in the K band at the 2σ level (nK -LBGs). The red error bars along with y-axis represent the permitted range of $\text{EW}(H\beta)$ estimated from the upper/lower limits on continuum flux density (see Section 4.3). The orange error bar with the arrow shows the SSA22-LBG-22 (the object without the detection of $H\beta$) and indicates the 3σ upper limit of $\text{EW}(H\beta)$. The black solid, dashed, dot-dashed, two dot-dashed lines show the model tracks for radiation-bounded nebulae, $Z = 0.004$, and constant star formation history from Zackrisson et al. (2013). The two black arrows at the right hand represents the influence of the dust attenuation. For LCG-1, the f_{esc} value estimated by the $\text{EW}(H\beta)$ – β method is roughly consistent with the f_{esc} value estimated from the direct LyC measurement.

density is obtained by extrapolating the UV spectral slope β from rest-frame UV to rest-frame optical wavelength. Except for special cases, the continuum flux density in the K -band will be similar to or higher than the extrapolation due to the Balmer break which is prominent for old stellar populations. In case of a strong nebular continuum with an extremely young and low-metallicity stellar population, the true continuum flux density can be lower than the extrapolation by $\Delta K \sim 0.3$ at most (e.g. Inoue 2011). Although LyC sources may have such an extreme stellar population, we believe that the extrapolation is a reasonable approximation of the lower limit on the continuum flux density. By using the upper and lower limits on the continuum flux density, we estimate the permitted range of $\text{EW}(H\beta)$ for SSA22-LBGs without the K -band detection. For SSA22-LBG-22 (the object without the detection of $H\beta$), we estimate the upper limit of $\text{EW}(H\beta)$ from the 3σ upper limit of the $H\beta$ line flux and the lower limit of the continuum flux density. The permitted range and the upper limit on $\text{EW}(H\beta)$ are also summarized in Table 3.

5 RESULTS FROM THE $\text{EW}(H\beta)$ – β DIAGRAM

Fig. 4 shows the result of the $\text{EW}(H\beta)$ – β method to constrain f_{esc} . In this diagram, we include the data for LCG-1, LCG-2, and the SSA22-LBGs listed in Table 3. The blue circles filled with cyan show our main targets, LCG-1 and LCG-2. The green diamonds with error bars represent UKIRT/ K -detected SSA22-LBGs (hereafter K -LBGs). The red error bars represent SSA22-LBGs, which are undetected in K at the 2σ level (hereafter nK -LBGs), whereas the horizontal error bars of the nK -LBGs represent the permitted range of $\text{EW}(H\beta)$ described

in Section 4.3. The uncertainty in β is indicated by the vertical error bars. For the sake of clarity, the error bars for β are placed at the left edge of the permitted range of $\text{EW}(\text{H}\beta)$. Therefore, the red error bars denote the expected regions in which the nK-LBGs are. The orange arrow with error bars represents SSA22-LBG-22 (the object without the detection of $\text{H}\beta$). The arrow denotes the upper limit on $\text{EW}(\text{H}\beta)$, estimated from the 3σ upper limit on the $\text{H}\beta$ flux and the lower limit on the continuum flux density.

In Fig. 4, we also show the model tracks for radiation-bounded nebulae with various f_{esc} , $Z = 0.004$, and constant SFH from Zackrisson et al. (2013). The model tracks are based on the *Yggdrasil* spectral synthesis code (Zackrisson et al. 2011), which simulates galaxy SEDs (stellar+nebular continuum emission and nebular emission lines) as a function of age for arbitrary SFHs. In Zackrisson et al. (2013) for the model tracks of $\text{EW}(\text{H}\beta)$ – β , the simple stellar population SED models are generated by Starburst99 (Leitherer et al. 1999) with Padova-AGB stellar evolutionary tracks (Vázquez & Leitherer 2005), assuming the Kroupa (2001) IMF with $[0.1 M_{\odot} - 100 M_{\odot}]$. The final galaxy SEDs are estimated by using the stellar SEDs integrated over the SFH as an input in the photoionization code CLOUDY (Ferland et al. 1998). The black solid, dashed, dot-dashed, and two dot-dashed lines represent the models with $f_{\text{esc}} = 0.0, 0.5, 0.7$, and 0.9 , respectively. Each model track changes with the production rate of ionizing photons in a galaxy, namely, the age of the stellar population. The age of the model galaxy increases from bottom left (1 Myr) to top right (300 Myr) along with each model track. Nebular continuum is already applied to these model tracks according to the f_{esc} values. As discussed in detail in Zackrisson et al. (2013, 2017), a different assumption of stellar populations (e.g. a different metallicity, SFH, IMF, and stellar evolutionary model) shifts the model tracks on the $\text{EW}(\text{H}\beta)$ – β diagram. While some alternative set of model parameters may be preferable for LCG-1 (and LCG-2/SSA22-LBGs), it is difficult to have a further discussion due to the large uncertainties in $\text{EW}(\text{H}\beta)$ and β . Therefore, we consider the simple assumption described above.

These models are for cases without any dust attenuation ($A_V = 0.0$), even though the observed LCGs/SSA22-LBGs are affected by dust, to various degree. The impact of dust on the $\text{EW}(\text{H}\beta)$ – β diagram depends on the dust attenuation curve and geometry of dust, gas and stars in the target galaxies (Zackrisson et al. 2013, 2017). The two black arrows on the right-hand panel of Fig. 4 represent two simple models for dust attenuation effects. In these simple models, we assume the Calzetti et al. (2000) attenuation curve. The black solid arrow is the case where the dust attenuation of the stellar component is the same as the attenuation of the nebular component ($A_V = A_{V,\text{neb}}$). Because the dust attenuation of the continuum and the emission line flux are the same, the arrow runs parallel to the y-axis. The black dashed arrow represents an alternative scenario where the dust attenuation of the stellar component is $0.44 \times$ the dust attenuation of the nebular component ($A_V = 0.44A_{V,\text{neb}}$). The relation between A_V and $A_{V,\text{neb}}$ has been discussed by e.g. Erb et al. (2006) and Kashino et al. (2013). According to these studies, the proportionality constant of the relation seems to range between 0.44 and 1.0 for high- z starbursts. Therefore, the two constant values adopted in our simple models represent reasonable assumptions.

Due to the blue UV spectral slope ($\beta \approx -2.5$) of LCG-1, we can directly compare its observed $\text{EW}(\text{H}\beta)$ and β values to the model prediction from Zackrisson et al. (2013) without considering the influence of dust attenuation. When taking the error bars in to account, we find that the $\text{EW}(\text{H}\beta)$ – β method indicates $f_{\text{esc}} = 0.0$ – 0.7 for the object LCG-1. As shown in Fig. 1, the direct LyC measurement also predicts a high f_{esc} value, $f_{\text{esc}} \gtrsim 0.5$, for this object. Hence, the

two methods give broadly consistent results. It is clear, however, that given the observational uncertainties, the $\text{EW}(\text{H}\beta)$ – β method would not be able to provide useful constraints on its own, as it is only able to rule out $f_{\text{esc}} > 0.7$ for this object.

For the remaining objects, it is difficult to directly apply the $\text{EW}(\text{H}\beta)$ – β method, since their UV slopes are redder and therefore likely more affected by dust. As an example, consider LCG-2, which displays $\beta \approx -1.4$. For this object, the dust-corrected (intrinsic) UV spectral slope, β_{int} , would be required for a detailed constraint on f_{esc} using the $\text{EW}(\text{H}\beta)$ – β model sequences. The intrinsic UV slope β_{int} could potentially be derived from SED fitting, although it would be premature to attempt this at the current time. For LBGs at $z \approx 4$, the SED-fitting analysis of Yamanaka & Yamada (2019) indicates $\beta_{\text{int}} \sim -2.5 \pm 0.3$ for objects with $\beta_{\text{obs}} \sim -1.4$. Since LBGs with the same β value at $z = 3$ and $z = 4$ are, on average, expected to be similar in terms of stellar populations, one could be tempted to shift LCG-2 to $\beta_{\text{int}} \sim -2.5 \pm 0.3$, in which case the $\text{EW}(\text{H}\beta)$ – β method would suggest $f_{\text{esc}} = 0.0$ – 0.5 . While this is formally consistent with the prediction from the direct LyC measurement ($f_{\text{esc}} \sim 0.0$), this would place the dust-corrected position of LCG-2 in the $\text{EW}(\text{H}\beta)$ – β diagram very close to the observed position of LCG-1, which would seem contradictory given that the direct LyC observations indicate significantly different f_{esc} for these two objects. Similar problems plague the $\text{EW}(\text{H}\beta)$ and β_{int} analysis of the other objects in Fig. 4 as well; because the other objects also display redder UV slopes (and have larger error bars), it is hard to provide constraints on f_{esc} from their positions expected from β_{int} in the $\text{EW}(\text{H}\beta)$ – β diagram at this stage. For the β_{int} estimation, it is required to conduct the detailed SED fitting analysis by using deep and multiband imaging data.

6 DISCUSSION

6.1 Probing the LyC escape mechanism

Throughout the paper, we have implicitly assumed f_{esc} estimated by the $\text{EW}(\text{H}\beta)$ – β method to be the same as that estimated from the direct LyC measurement. It is, however, possible that this assumption may break down in the case where the escape of LyC photons is anisotropic.

Because the direct LyC measurement depends on the optical depth of neutral hydrogen along the line of sight, the direct method displays a dependence on the viewing angle. The $\text{EW}(\text{H}\beta)$ – β method, on the other hand, does not have the same angular dependence. In the scenario of a radiation-bounded nebula with holes (Zackrisson et al. 2013), also known as the picket-fence model, the LyC photons escape from the galaxy through holes or tunnels of optically thin (or almost ionized) hydrogen gas. However, the distribution of these holes and their sizes may differ across the object, and the ones facing the observer (responsible for the leakage of LyC photons detected in direct observations) may not be representative of the average across the whole galaxy. If this is the case, direct and indirect methods may not necessarily result in comparable f_{esc} estimates.

Indeed, recent observations indicate that the LyC photons from LCGs with high f_{esc} may have escaped through low-density channels of the type envisioned in the radiation-bounded nebula with holes scenario (Vanzella et al. 2016, 2018, 2019; Izotov et al. 2018b). According to Verhamme et al. (2015) and Behrens, Dijkstra & Niemeyer (2014), a triple-peaked Ly α emission profile with a peak at its systemic velocity (or a double-peaked Ly α emission profile with a small peak separation) is predicted for high f_{esc} LCGs in this scenario, and such a spectral feature has indeed been observed in some previous works (Vanzella et al. 2018, 2019). Moreover, Rivera-

Thorsen et al. (2019) report on the LyC properties and f_{esc} properties of the multiple images from the gravitationally lensed SFG at $z = 2.4$. The individual images of the LyC source in this object are spatially unresolved within the high-resolution *HST* image, which may indicate narrow escape channels.

If LyC leakage through a radiation-bounded nebular with holes is a commonly occurring phenomenon, the EW(H β)- β method could become an important tool for probing the ‘angle-averaged’ (hereafter global) escape fraction. As mentioned in Section 5, the EW(H β)- β method does display a dependence on dust (the dust attenuation curve and the geometry of dust, gas, and stars), and hence on the viewing angle. However, this angular dependence on dust is relatively weaker than the angular dependence of the direct LyC measurements on neutral hydrogen because the dust opacity in the optical/UV wavelength is much smaller than the opacity of neutral hydrogen for LyC photons. On the other hand, the dust opacity for LyC photons in ionized gas can be important (Chisholm et al. 2018; Steidel et al. 2018; Gazagnes et al. 2020; see also Inoue, Hirashita & Kamaya 2001; Inoue 2001, 2002).⁷ In any case, the angular dependence on dust is much weaker when considering SFGs with little dust attenuation like LCG-1 that displays the blue UV slope β . When assessing the role of galaxies in the reionization of the Universe, it is in fact the global f_{esc} that matters, not f_{esc} in the direction of the observer (which would be measured by the direct LyC measurements).

By combining direct measurements of LyC escape (which trace optically thin holes or regions) with indirect ones (which may potentially provide a better estimate of the global f_{esc}) for the same objects, it may be possible to quantitatively assess the anisotropy of the leakage, at least in the case of SFGs at $z = 3$ –4 and for lower-redshift analogues. The ultimate goal is to understand the LyC escape mechanism of SFGs in the epoch of reionization ($z > 6$) that are predicted to have a little amount of dust attenuation. Therefore, it is worth investigating the difference of the direct and indirect measurements of LyC escape for the lower-redshift analogues of the reionization-epoch SFGs. It should be stressed, however, that one can only hope to detect very extreme cases of LyC leakage ($f_{\text{esc}} \gtrsim 0.5$) using the EW(H β)- β method. Similar indirect techniques that make use of a wider set of spectroscopic data could in principle do better (Jensen et al. 2016; Giri et al. 2020).

6.2 Uncertainties in EW(H β)- β method

Here, we discuss the observational effects that dominate the uncertainties in the EW(H β)- β method, and how the errors may potentially be reduced in the future. In our analysis, the errors on EW(H β) and β are dominated by the uncertainties in the broad-band photometry at the longer wavelengths, namely, in the Subaru/ z' , y , and

⁷The cross-section of neutral hydrogen to LyC is $\sigma_{\text{H I}} = 6.3 \times 10^{-18} \text{ cm}^2$. The cross-section of dust is $\sigma_{\text{dust}} = \pi \times 10^{-10} \text{ cm}^2$, assuming the radius of dust grain $r = 0.1 \text{ }\mu\text{m}$ and the dust absorption coefficient $Q = 1$. The dust-to-hydrogen (atomic+molecular) mass ratio is $D = (m_{\text{dust}}N_{\text{dust}})/(\mu m_{\text{H}}N_{\text{H}}) = (m_{\text{dust}}N_{\text{dust}})/(\mu m_{\text{H}}N_{\text{H I}}/X_{\text{H I}})$, where μ is the mean molecular weight and $X_{\text{H I}}$ is the neutral fraction of hydrogen. Assuming the dust mass density $\rho = 3 \text{ g cm}^{-3}$ and $\mu = 1.4$, the dust-to-hydrogen mass ratio is $D = 5.37 \times 10^9 X_{\text{H I}}(N_{\text{dust}}/N_{\text{H I}})$. Consequently, the ratio of the opacities of H I and dust is $k_{\text{H I}}/k_{\text{dust}} = (\sigma_{\text{H I}}N_{\text{H I}})/(\sigma_{\text{dust}}N_{\text{dust}}) \sim 100 X_{\text{H I}}/D$. According to Draine et al. (2007), the dust-to-hydrogen mass ratio of Milky Way is 7.3×10^{-3} , which indicates $k_{\text{H I}}/k_{\text{dust}} \sim 1.5 \times 10^4 X_{\text{H I}}$. Although the dust opacity for LyC is negligible in neutral gas, the opacity is not negligible in ionized regions ($X_{\text{H I}} < 1$).

UKIRT/*K*-band filters. Since the spectroscopic H β flux is well determined (with a typical uncertainty of $\lesssim 10$ per cent; Table 3), the uncertainty on EW(H β) is attributed to the large uncertainty in the continuum flux density estimated from the UKIRT/*K*-band photometry.

For blue UV spectral slopes ($\beta < -2.0$), the z' - and y -band fluxes become fainter than those of the *R* and *i* bands. Therefore, the uncertainty on the z' - and y -band photometry is critical for the β estimation. If we were to obtain much deeper images of z' , y , and *K* band in the SSA22 field, the EW(H β)- β would be easier to apply.

A similar issue may also be important for attempts to apply the EW(H β)- β method to SFGs at $z > 6$. Since strong nebular emission lines are expected for SFGs at $z > 6$ (e.g. Harikane et al. 2018), emission line identification may be easily accomplished by future instruments such as *JWST*. However, if the H β continuum is undetected in the spectroscopic data, as would be expected for very faint sources and/or observations at high spectral resolution, deep imaging observations may none the less be important to measure the continuum flux.

The complicated effects of dust on the EW(H β)- β diagram also adds substantial uncertainty in the application of the EW(H β)- β method for estimating f_{esc} . The observational data in Fig. 4 are affected by dust, whereas the model sequences from Zackrisson et al. (2013) are for *intrinsic* EW(H β) and β prior to dust attenuation. Both the attenuation curve and the amount of dust attenuation are critical parameters in the exercise for applying the right corrections to EW(H β) and β . As mentioned in Section 5, if the dust attenuation applied for the nebular component is different from that for the stellar component, the observational data points of the EW(H β)- β diagram shift diagonally from bottom left to top right as the amount of the dust attenuation is increased.

For LCG-1 (and some SSA22-LBGs), however, the observed UV spectral slope is $\beta \approx -2.5$, which is quite blue compared to the average β value of LBGs/LAEs at similar redshifts ($\beta \sim -1.7$ or -2.0 for $M_{\text{UV}} \sim -21.0$ at $z \sim 3$; e.g. Bouwens et al. 2009; Santos et al. 2019). Due to the strong dependence of β on the dust attenuation (e.g. Meurer, Heckman & Calzetti 1999), these blue UV spectral slopes β indicate that dust reddening must be small. Therefore, the observed EW(H β) and β are expected to be close to their intrinsic values, at least for LCG-1 and possibly also for some of the other SSA22-LBGs in our sample.

7 CONCLUSION

In this work, we examine the validity of the EW(H β)- β method proposed by Zackrisson et al. (2013) to indirectly estimates the escape fraction of LyC photons from individual galaxies. For this purpose, we conduct *K*-band multiobject spectroscopy with Keck/MOSFIRE to measure the H β emission line flux of LCGs, LBGs, and LAEs at $z \sim 3.0$ –3.5 in the SSA22 field. Thanks to the unique Subaru/*NB359* filter, we can also directly detect the LyC flux from these objects and assess the associated escape fraction f_{esc} . Finally, we compare the outcomes of these two methods and discuss the usefulness of combining direct and indirect methods for probing the astrophysical mechanism that allow LyC photons to escape from galaxies.

Our main conclusions can be summarized as follows:

(i) We reconfirm the spectroscopic redshift and measure the H β emission-line flux from two LCGs and six SSA22-LBGs. The spectroscopic redshifts of our main targets, LCG-1 and LCG-2, are $z_{\text{spec}} = 3.2890$ and 3.3152 , in good agreement with the Ly α redshift values reported by Micheva et al. (2017b).

(ii) When plotting our 8 LCGs/SSA22-LBGs on to the EW(H β)- β diagram, we find LCG-1 to be suitably located for assessing f_{esc}

using the Zackrisson et al. (2013) method. Based on the model predictions, we infer $f_{\text{esc}} = 0.0\text{--}0.7$ for this object. While this is broadly consistent with the escape fraction estimated from the directly detected LyC flux of this object ($f_{\text{esc}} \approx 0.5$), the large error bars on β and EW(H β) prevent us from setting strong quantitative constraints on the agreement. The remaining objects display UV continuum slopes β that are too red to allow any meaningful comparison without the application of dust corrections to the β slopes.

(iii) We discuss the possibility that direct and indirect LyC leakage estimates could return discrepant estimates of f_{esc} in the case of anisotropic LyC leakage, as in the case where LyC leakage happens through a radiation-bounded nebula with holes. In this scenario, the direct LyC measurements trace the covering fraction along the line of sight. This quantity may differ from the angle-averaged, ‘global’ escape fraction that matters for the role of galaxies in the reionization of the Universe, and which could potentially be better probed through indirect f_{esc} -estimation techniques like the EW(H β)- β method. Hence, improved comparisons between these two techniques for SFGs at $z = 3\text{--}4$ and low- z analogues could provide useful constraints on the anisotropy of LyC leakage.

ACKNOWLEDGEMENTS

SY and AKI was supported by JSPS KAKENHI grant no. 17H01114. TH was supported by Leading Initiative for Excellent Young Researchers, MEXT, Japan. EZ acknowledges funding from the Swedish National Space Board. The data presented herein were obtained at the W. M. Keck Observatory, which is operated as a scientific partnership among the California Institute of Technology, the University of California, and the National Aeronautics and Space Administration. The Observatory was made possible by the generous financial support of the W. M. Keck Foundation. This work is based on data collected at Subaru Telescope, which is operated by the National Astronomical Observatory of Japan. The UKIDSS project is defined in Lawrence et al. (2007). UKIDSS uses the UKIRT Wide Field Camera (WFCAM; Casali et al. 2007). The photometric system is described in Hewett et al. (2006), and the calibration is described in Hodgkin et al. (2009). The pipeline processing and science archive are described in Irwin et al. in preparation and Hambly et al. (2008). We use UKIDSS data release 10. Data analysis was in part carried out on the Multi-wavelength Data Analysis System operated by the Astronomy Data Center (ADC), National Astronomical Observatory of Japan. The authors wish to recognize and acknowledge the very significant cultural role and reverence that the summit of Maunakea has always had within the indigenous Hawaiian community. We are most fortunate to have the opportunity to conduct observations from this mountain.

DATA AVAILABILITY

The data underlying this article will be shared on reasonable request to the corresponding author.

REFERENCES

Aihara H. et al., 2018, *PASJ*, 70, S8
 Behrens C., Dijkstra M., Niemeyer J. C., 2014, *A&A*, 563, A77
 Bergvall N., Zackrisson E., Andersson B. G., Arnberg D., Masegosa J., Östlin G., 2006, *A&A*, 448, 513
 Bertin E., Arnouts S., 1996, *A&AS*, 117, 393
 Bian F., Fan X., McGreer I., Cai Z., Jiang L., 2017, *ApJ*, 837, L12
 Bolzonella M., Miralles J. M., Pelló R., 2000, *A&A*, 363, 476

Borthakur S., Heckman T. M., Leitherer C., Overzier R. A., 2014, *Science*, 346, 216
 Boulade O. et al., 2003, Instrument Design and Performance for Optical/Infrared Ground-based Telescopes, Vol. 4841. SPIE, p. 72
 Bouwens R. J. et al., 2009, *ApJ*, 705, 936
 Bouwens R. J. et al., 2014, *ApJ*, 793, 115
 Bouwens R. J., Smit R., Labbé I., Franx M., Caruana J., Oesch P., Stefanon M., Rasappu N., 2016, *ApJ*, 831, 176
 Calzetti D., Kinney A. L., Storchi-Bergmann T., 1994, *ApJ*, 429, 582
 Calzetti D., Armus L., Bohlin R. C., Kinney A. L., Koornneef J., Storchi-Bergmann T., 2000, *ApJ*, 533, 682
 Casali M. et al., 2007, *A&A*, 467, 777
 Chisholm J. et al., 2018, *A&A*, 616, A30
 Cowie L. L., Lilly S. J., Gardner J., McLean I. S., 1988, *ApJ*, 332, L29
 de Barros S. et al., 2016, *A&A*, 585, A51
 Dijkstra M., Gronke M., Venkatesan A., 2016, *ApJ*, 828, 71
 Draine B. T. et al., 2007, *ApJ*, 663, 866
 Erb D. K., Steidel C. C., Shapley A. E., Pettini M., Reddy N. A., Adelberger K. L., 2006, *ApJ*, 647, 128
 Faber S. M. et al., 2003, Instrument Design and Performance for Optical/Infrared Ground-based Telescopes, Vol. 4841. SPIE, p. 1657
 Fan X. et al., 2006, *AJ*, 132, 117
 Fan X., Narayanan V. K., Strauss M. A., White R. L., Becker R. H., Pentericci L., Rix H.-W., 2002, *AJ*, 123, 1247
 Fazio G. G. et al., 2004, *ApJS*, 154, 10
 Ferland G. J., Korista K. T., Verner D. A., Ferguson J. W., Kingdon J. B., Verner E. M., 1998, *PASP*, 110, 761
 Finkelstein S. L. et al., 2012, *ApJ*, 756, 164
 Finkelstein S. L. et al., 2015, *ApJ*, 810, 71
 Finkelstein S. L. et al., 2019, *ApJ*, 879, 36
 Fletcher T. J., Tang M., Robertson B. E., Nakajima K., Ellis R. S., Stark D. P., Inoue A., 2019, *ApJ*, 878, 87
 Freeman W. R. et al., 2019, *ApJ*, 873, 102
 Fukugita M., Ichikawa T., Gunn J. E., Doi M., Shimasaku K., Schneider D. P., 1996, *AJ*, 111, 1748
 Gazagnes S., Chisholm J., Schaerer D., Verhamme A., Izotov Y., 2020, *A&A*, 639, A85
 Giri S. K., Zackrisson E., Binggeli C., Pelckmans K., Cubo R., 2020, *MNRAS*, 491, 5277
 Grazian A. et al., 2016, *A&A*, 585, A48
 Greiner J. et al., 2009, *ApJ*, 693, 1610
 Hambly N. C. et al., 2008, *MNRAS*, 384, 637
 Harikane Y. et al., 2018, *ApJ*, 859, 84
 Hayashino T. et al., 2004, *AJ*, 128, 2073
 Hewett P. C., Warren S. J., Leggett S. K., Hodgkin S. T., 2006, *MNRAS*, 367, 454
 Hodgkin S. T., Irwin M. J., Hewett P. C., Warren S. J., 2009, *MNRAS*, 394, 675
 Ichikawa T. et al., 2006, Ground-based and Airborne Instrumentation for Astronomy, Vol. 6269. SPIE, p. 626916
 Inoue A. K., 2001, *AJ*, 122, 1788
 Inoue A. K., 2002, *ApJ*, 570, 688
 Inoue A. K., 2011, *MNRAS*, 415, 2920
 Inoue A. K., Iwata I., 2008, *MNRAS*, 387, 1681
 Inoue A. K., Hirashita H., Kamaya H., 2001, *ApJ*, 555, 613
 Inoue A. K., Iwata I., Deharveng J. M., Buat V., Burgarella D., 2005, *A&A*, 435, 471
 Inoue A. K., Iwata I., Deharveng J.-M., 2006, *MNRAS*, 371, L1
 Inoue A. K., Shimizu I., Iwata I., Tanaka M., 2014, *MNRAS*, 442, 1805
 Itoh R. et al., 2018, *ApJ*, 867, 46
 Iwata I. et al., 2009, *ApJ*, 692, 1287
 Iwata I., Inoue A. K., Micheva G., Matsuda Y., Yamada T., 2019, *MNRAS*, 488, 5671
 Izotov Y. I., Schaerer D., Thuan T. X., Worseck G., Guseva N. G., Orlitová I., Verhamme A., 2016a, *MNRAS*, 461, 3683
 Izotov Y. I., Orlitová I., Schaerer D., Thuan T. X., Verhamme A., Guseva N. G., Worseck G., 2016b, *Nature*, 529, 178
 Izotov Y. I., Schaerer D., Worseck G., Guseva N. G., Thuan T. X., Verhamme A., Orlitová I., Fricke K. J., 2018a, *MNRAS*, 474, 4514

- Izotov Y. I., Worseck G., Schaerer D., Guseva N. G., Thuan T. X., Fricke Verhamme A., Orlitová I., 2018b, *MNRAS*, 478, 4851
- Jensen H., Zackrisson E., Pelckmans K., Binggeli C., Ausmees K., Lundholm U., 2016, *ApJ*, 827, 5
- Kashikawa N. et al., 2006, *ApJ*, 648, 7
- Kashikawa N. et al., 2011, *ApJ*, 734, 119
- Kashino D. et al., 2013, *ApJ*, 777, L8
- Konno A. et al., 2018, *PASJ*, 70, S16
- Kroupa P., 2001, *MNRAS*, 322, 231
- Kubo M., Yamada T., Ichikawa T., Kajisawa M., Matsuda Y., Tanaka I., 2015, *ApJ*, 799, 38
- Kulkarni G., Worseck G., Hennawi J. F., 2019, *MNRAS*, 488, 1035
- Lawrence A. et al., 2007, *MNRAS*, 379, 1599
- Lee K.-G. et al., 2014, *ApJ*, 795, L12
- Lee K.-G. et al., 2018, *ApJS*, 237, 31
- Leitet E., Bergvall N., Piskunov N., Andersson B. G., 2011, *A&A*, 532, A107
- Leitet E., Bergvall N., Hayes M., Linné S., Zackrisson E., 2013, *A&A*, 553, A106
- Leitherer C. et al., 1999, *ApJS*, 123, 3
- Lilly S. J., Cowie L. L., Gardner J. P., 1991, *ApJ*, 369, 79
- Madau P., Haardt F., 2015, *ApJ*, 813, L8
- Madau P., Haardt F., Rees M. J., 1999, *ApJ*, 514, 648
- Matsuda Y. et al., 2004, *AJ*, 128, 569
- Matsuoka Y. et al., 2018, *ApJ*, 869, 150
- McLean I. S. et al., 2010, Ground-based and Airborne Instrumentation for Astronomy III, Vol. 7735. SPIE, p. 77351E
- McLean I. S. et al., 2012, Ground-based and Airborne Instrumentation for Astronomy IV, Vol. 8446. SPIE, p. 84460J
- Meurer G. R., Heckman T. M., Calzetti D., 1999, *ApJ*, 521, 64
- Micheva G., Iwata I., Inoue A. K., 2017a, *MNRAS*, 465, 302
- Micheva G., Iwata I., Inoue A. K., Matsuda Y., Yamada T., Hayashino T., 2017b, *MNRAS*, 465, 316
- Miyazaki S. et al., 2002, *PASJ*, 54, 833
- Miyazaki S. et al., 2012, Ground-based and Airborne Instrumentation for Astronomy IV, Vol. 8446. SPIE, p. 84460Z
- Miyazaki S. et al., 2018, *PASJ*, 70, S1
- Mostardi R. E., Shapley A. E., Nestor D. B., Steidel C. C., Reddy N. A., Trainor R. F., 2013, *ApJ*, 779, 65
- Mostardi R. E., Shapley A. E., Steidel C. C., Trainor R. F., Reddy N. A., Siana B., 2015, *ApJ*, 810, 107
- Naidu R. P. et al., 2017, *ApJ*, 847, 12
- Nakajima K., Ouchi M., 2014, *MNRAS*, 442, 900
- Nakajima K., Ouchi M., Shimasaku K., Hashimoto T., Ono Y., Lee J. C., 2013, *ApJ*, 769, 3
- Nakajima K., Ellis R. S., Robertson B. E., Tang M., Stark D. P., 2020, *ApJ*, 889, 161
- Nakamura E., Inoue A. K., Hayashino T., Horie M., Kousai K., Fujii T., Matsuda Y., 2011, *MNRAS*, 412, 2579
- Nestor D. B., Shapley A. E., Steidel C. C., Siana B., 2011, *ApJ*, 736, 18
- Nestor D. B., Shapley A. E., Kornei K. A., Steidel C. C., Siana B., 2013, *ApJ*, 765, 47
- Oke J. B., Gunn J. E., 1983, *ApJ*, 266, 713
- Ono Y. et al., 2012, *ApJ*, 744, 83
- Ouchi M. et al., 2010, *ApJ*, 723, 869
- Ouchi M. et al., 2018, *PASJ*, 70, S13
- Paardekooper J.-P., Khochfar S., Dalla Vecchia C., 2015, *MNRAS*, 451, 2544
- Planck Collaboration et al., 2016, *A&A*, 596, A108
- Rivera-Thorsen T. E. et al., 2019, *Science*, 366, 738
- Robertson B. E., Ellis R. S., Furlanetto S. R., Dunlop J. S., 2015, *ApJ*, 802, L19
- Rogers A. B., McLure R. J., Dunlop J. S., 2013, *MNRAS*, 429, 2456
- Salpeter E. E., 1955, *ApJ*, 121, 161
- Santos S. et al., 2020, *MNRAS*, 493, 141
- Schenker M. A., Stark D. P., Ellis R. S., Robertson B. E., Dunlop J. S., McLure R. J., Kneib J.-P., Richard J., 2012, *ApJ*, 744, 179
- Shapley A. E., Steidel C. C., Strom A. L., Bogosavljević M., Reddy N. A., Siana B., Mostardi R. E., Rudie G. C., 2016, *ApJ*, 826, L24
- Siana B. et al., 2007, *ApJ*, 668, 62
- Siana B. et al., 2010, *ApJ*, 723, 241
- Siana B. et al., 2015, *ApJ*, 804, 17
- Steidel C. C. et al., 2014, *ApJ*, 795, 165
- Steidel C. C., Adelberger K. L., Dickinson M., Giavalisco M., Pettini M., Kellogg M., 1998, *ApJ*, 492, 428
- Steidel C. C., Adelberger K. L., Shapley A. E., Pettini M., Dickinson M., Giavalisco M., 2000, *ApJ*, 532, 170
- Steidel C. C., Pettini M., Adelberger K. L., 2001, *ApJ*, 546, 665
- Steidel C. C., Adelberger K. L., Shapley A. E., Pettini M., Dickinson M., Giavalisco M., 2003, *ApJ*, 592, 728
- Steidel C. C., Erb D. K., Shapley A. E., Pettini M., Reddy N., Bogosavljević M., Rudie G. C., Rakic O., 2010, *ApJ*, 717, 289
- Steidel C. C., Bogosavljević M., Shapley A. E., Reddy N. A., Rudie G. C., Pettini M., Trainor R. F., Strom A. L., 2018, *ApJ*, 869, 123
- Suzuki R., Tokoku C., Ichikawa T., Nishimura T., 2003, Instrument Design and Performance for Optical/Infrared Ground-based Telescopes, Vol. 4841. SPIE, p. 307
- Tamura Y. et al., 2009, *Nature*, 459, 61
- Tanvir N. R. et al., 2019, *MNRAS*, 483, 5380
- Totani T., Kawai N., Kosugi G., Aoki K., Yamada T., Iye M., Ohta K., Hattori T., 2006, *PASJ*, 58, 485
- Totani T., Aoki K., Hattori T., Kawai N., 2016, *PASJ*, 68, 15
- Umehata H. et al., 2014, *MNRAS*, 440, 3462
- Vanzella E. et al., 2010b, *ApJ*, 725, 1011
- Vanzella E. et al., 2016, *ApJ*, 825, 41
- Vanzella E. et al., 2018, *MNRAS*, 476, L15
- Vanzella E. et al., 2020, *MNRAS*, 491, 1093
- Vanzella E., Siana B., Cristiani S., Nonino M., 2010a, *MNRAS*, 404, 1672
- Vasei K. et al., 2016, *ApJ*, 831, 38
- Vázquez G. A., Leitherer C., 2005, *ApJ*, 621, 695
- Verhamme A., Orlitová I., Schaerer D., Hayes M., 2015, *A&A*, 578, A7
- Verhamme A., Orlitová I., Schaerer D., Izotov Y., Worseck G., Thuan T. X., Guseva N., 2017, *A&A*, 597, A13
- Wilkins S. M., Bunker A., Coulton W., Croft R., di Matteo T., Khandai N., Feng Y., 2013, *MNRAS*, 430, 2885
- Wise J. H., Demchenko V. G., Halicek M. T., Norman M. L., Turk M. J., Abel T., Smith B. D., 2014, *MNRAS*, 442, 2560
- Yajima H., Choi J.-H., Nagamine K., 2011, *MNRAS*, 412, 411
- Yamada T., Nakamura Y., Matsuda Y., Hayashino T., Yamauchi R., Morimoto N., Kousai K., Umemura M., 2012a, *AJ*, 143, 79
- Yamada T., Matsuda Y., Kousai K., Hayashino T., Morimoto N., Umemura M., 2012b, *ApJ*, 751, 29
- Yamanaka S., Yamada T., 2019, *PASJ*, 71, 51
- Zackrisson E. et al., 2017, *ApJ*, 836, 78
- Zackrisson E., Rydberg C.-E., Schaerer D., Östlin G., Tuli M., 2011, *ApJ*, 740, 13
- Zackrisson E., Inoue A. K., Jensen H., 2013, *ApJ*, 777, 39
- Zahn O. et al., 2012, *ApJ*, 756, 65

APPENDIX: REDUCED 2D IMAGES AND 1D SPECTRA OF ALL OUR TARGETS

We here show all the reduced 2D spectra image and the successfully extracted 1D spectra in Fig. A1. In cases where the 1D spectrum is not extracted, we only show the 2D spectral image. In Tables A1 and A2, we show the results of the flux measurements. The following is brief comments on some SSA22-LBGs listed in Table A2 (objects with the detection of just a single emission line), i.e. SSA22-LBG-05, SSA22-LBG-13, and Y12LAE-3.

A.1 SSA22-LBG-05

This object is observed by Keck/DEIMOS under the SSA22HIT project. The spectroscopic redshift is $z_{\text{spec, Ly } \alpha} = 3.112$ which is measured from the DEIMOS observation for the Ly α emission line.

Table A1. Summary of flux measurement for LCG-1, LCG-2, and the SSA22-LBGs with the detection of >2 emission lines.

Name	z_{spec}^a	[O III] λ 5007			[O III] λ 4959			$\text{H}\beta^f$		
		λ^b	FWHM ^c	Total flux ^d	$\lambda^{b,e}$	FWHM ^c	Total flux ^d	$\lambda^{b,e}$	FWHM ^c	Total flux ^d
Mask-1										
LCG-1	3.2890	21480.1	248.0	112.57 ± 0.77	21274.5	233.9	38.05 ± 0.87	20855.8	282.7	19.82 ± 0.96
SSA22-LBG-01	3.0892	20479.9	145.1	72.91 ± 0.68	20283.9	155.1	23.99 ± 1.11	19884.7	161.8	11.72 ± 0.64
SSA22-LBG-02	3.3437	21754.0	205.7	60.36 ± 0.86	21545.8	245.5	21.77 ± 1.13	21121.8	211.4	10.36 ± 0.68
SSA22-LBG-06	3.1098	20583.0	144.7	15.78 ± 1.24	20386.0	182.6	5.24 ± 0.51	19984.8	–	–
SSA22-LBG-08	3.3327	21699.3	131.6	22.34 ± 0.64	21491.6	112.5	6.26 ± 0.45	21068.6	–99	–99
SSA22-LBG-09	2.9768	19916.5	179.8	121.30 ± 0.96	19725.9	184.0	40.07 ± 0.99	19337.7	276.3	13.75 ± 1.64
SSA22-LBG-10	3.2013	21040.9	214.2	44.14 ± 1.08	20839.4	223.6	16.68 ± 0.85	20429.3	188.8	14.25 ± 0.61
SSA22-LBG-12	3.1118	20592.8	172.3	171.40 ± 0.88	20395.7	171.1	58.25 ± 0.68	19994.3	166.4	27.72 ± 1.31
SSA22-LBG-16	3.1041	20554.2	105.1	13.24 ± 1.16	20357.5	167.1	4.42 ± 0.42	19956.8	156.7	4.32 ± 0.58
SSA22-LBG-17	3.0734	20400.3	166.3	51.37 ± 0.75	20205.0	186.9	18.78 ± 1.10	19807.4	–	–
Y12LAE-1	3.0824	20445.6	100.9	8.14 ± 0.38	20249.8	173.7	4.56 ± 0.56	19851.3	–	–
Mask-2										
LCG-2	3.3152	21611.3	309.5	140.57 ± 3.11	21404.4	335.4	54.60 ± 4.41	20983.2	340.9	53.86 ± 3.10
SSA22-LBG-09	2.9772	19918.7	178.8	117.95 ± 2.40	19728.0	201.8	39.83 ± 3.05	19339.8	–	–
SSA22-LBG-12	3.1116	20591.9	210.4	136.47 ± 2.19	20394.8	118.1	26.19 ± 1.05	19993.5	–	–
SSA22-LBG-22	3.3490	21780.9	122.2	16.37 ± 1.24	21572.4	113.2	6.86 ± 1.44	21147.9		<2.19

^a z_{spec} is estimated from the [O III] $\lambda 5007$ emission line.^b Centre of Gaussian function in units of Å.^c FWHM of Gaussian function in units of km s^{-1} . FWHM is not corrected for the instrumental broadening.^d Total flux in units of $10^{-18} \text{ erg s}^{-1} \text{ cm}^{-2}$.^e The centre wavelength of [O III] $\lambda 4959$ and $\text{H}\beta$ are calculated from z_{spec} and their vacuum wavelength. They are fixed in the flux measurement.^f ‘–’ indicates that the predicted wavelength is the outside of the wavelength coverage of our MOSFIRE observation.

‘–99’ indicates that the predicted wavelength is strongly affected by OH night sky lines.

The symbol of ‘<’ indicates a 3σ upper-limit.**Table A2.** Summary of flux measurement for SSA22-LBGs with the detection of a single emission line.

Name	Unidentified emission line			Comment
	λ^a	FWHM ^b	Total flux ^c	
Mask-1				
SSA22-LBG-04	22757.1	195.7	45.37 ± 1.69	Line profile looks like [O II] λλ3726, 3729 doublet.
SSA22-LBG-05	20611.2	182.5	32.32 ± 0.54	Observed by Keck/DEIMOS under SSA22HIT project.
SSA22-LBG-07	21148.2	235.9	59.75 ± 0.79	
SSA22-LBG-13	23828.9	73.1	12.19 ± 2.57	Observed by Keck/DEIMOS under SSA22HIT project.
SSA22-LBG-15	19414.4	281.1	15.09 ± 1.73	
Mask-2				
SSA22-LBG-26	19370.5	201.1	52.54 ± 3.21	
SSA22-LBG-31	21693.0	159.2	27.70 ± 1.93	
Y12LAE-3	20607.5	174.9	21.39 ± 1.15	Suppose line is [O III] λ5007, z_{spec} is consistent with z_{phot} of Y12LAEs.

^a Centre of Gaussian function in units of Å.^b FWHM of Gaussian function in units of km s^{-1} . FWHM is not corrected for the instrumental broadening.^c Total flux in units of $10^{-18} \text{ erg s}^{-1} \text{ cm}^{-2}$.

If assuming the single emission line detected by our MOSFIRE observation is [O III] $\lambda 5007$, the spectroscopic redshift is $z_{\text{spec}, [\text{O III}]} = 3.1154$. Since the spectroscopic redshift is consistent in the observations, SSA22-LBG-05 is actually a redshift-confirmed object. However, the $\text{H}\beta$ wavelength is not covered by our observation due to the MOSFIRE slitlet configuration. Therefore, this object is not used for our analysis.

A.2 SSA22-LBG-13

This object is observed by Keck/DEIMOS under the SSA22HIT project. The spectroscopic redshift is $z_{\text{spec}, \text{Ly}\alpha} = 2.869$. If assuming the single emission line detected by our MOSFIRE observation is [O III] $\lambda 5007$ or $\text{H}\alpha$ ($\lambda_{\text{vac}} = 6564.61$), the spectroscopic redshift is $z_{\text{spec}, [\text{O III}]} = 3.7580$ or $z_{\text{spec}, \text{H}\alpha} = 2.6299$, respectively. The spectro-

scopic redshift is not consistent in the observations. Therefore, this object is still a unidentified object.

A.3 Y12LAE-3

This object is taken from the LAE candidates at $z_{\text{phot}} = 3.1$ studied in Yamada et al. (2012a), although the narrow-band excess was below their criteria for the robust LAE sample. If assuming the single emission line detected by our MOSFIRE observation is [O III] $\lambda 5007$, the spectroscopic redshift is $z_{\text{spec}, [\text{O III}]} = 3.1147$. Since the spectroscopic redshift is consistent with the photometric redshift, Y12LAE-3 is a new redshift-confirmed object by our observation. However, the $\text{H}\beta$ wavelength is not covered by our observation due to the MOSFIRE slitlet configuration. Therefore, this object is not used for our analysis.

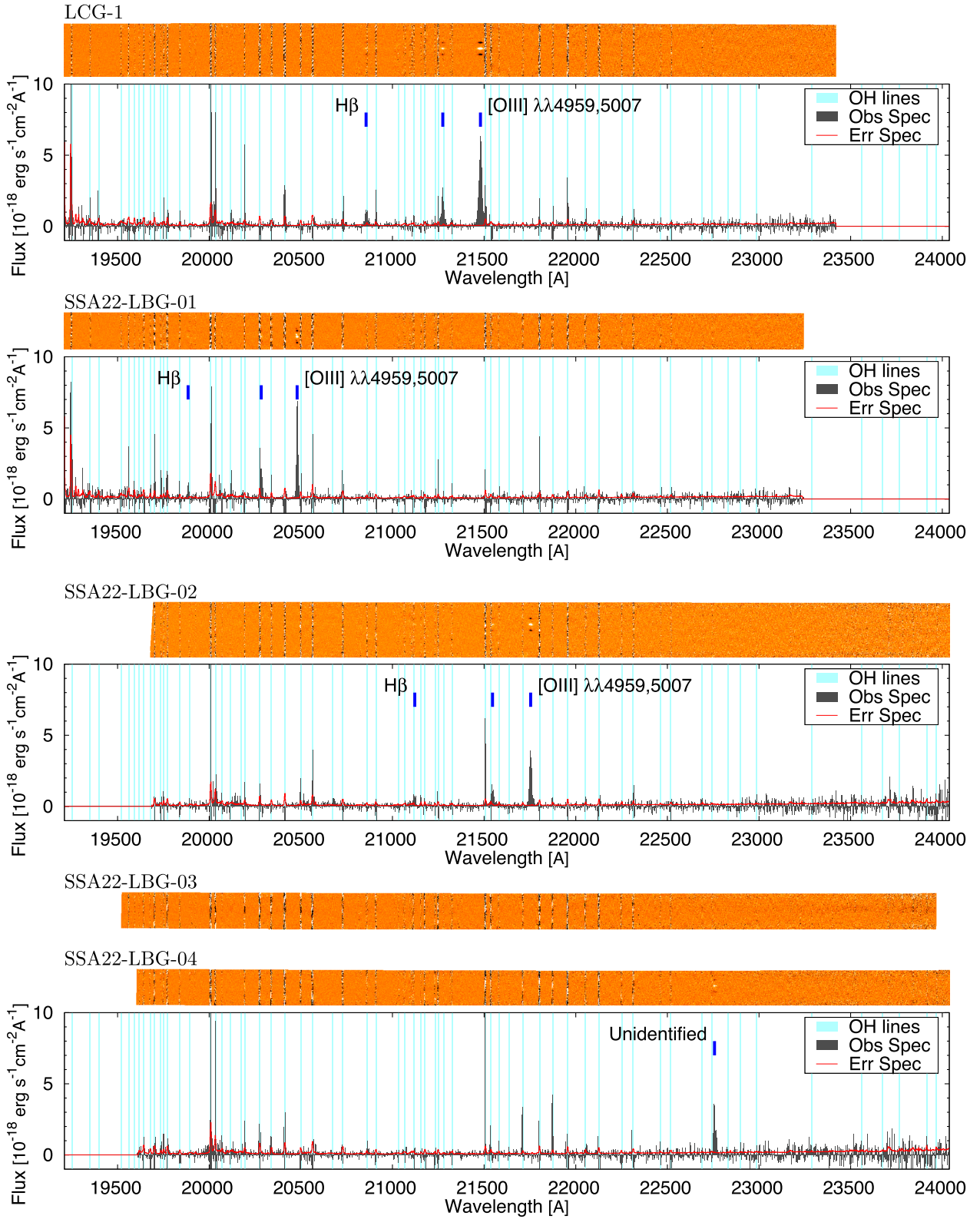
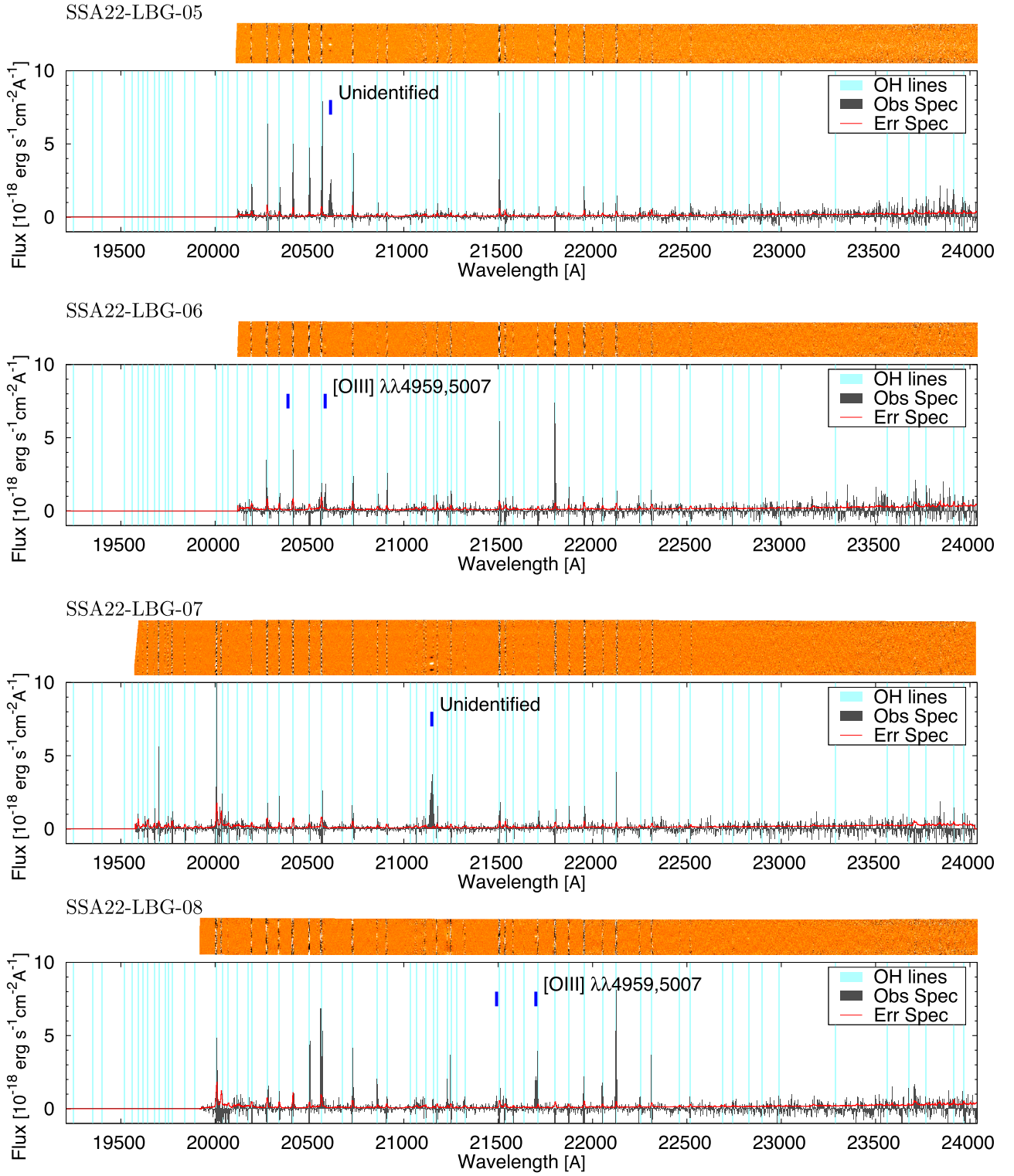
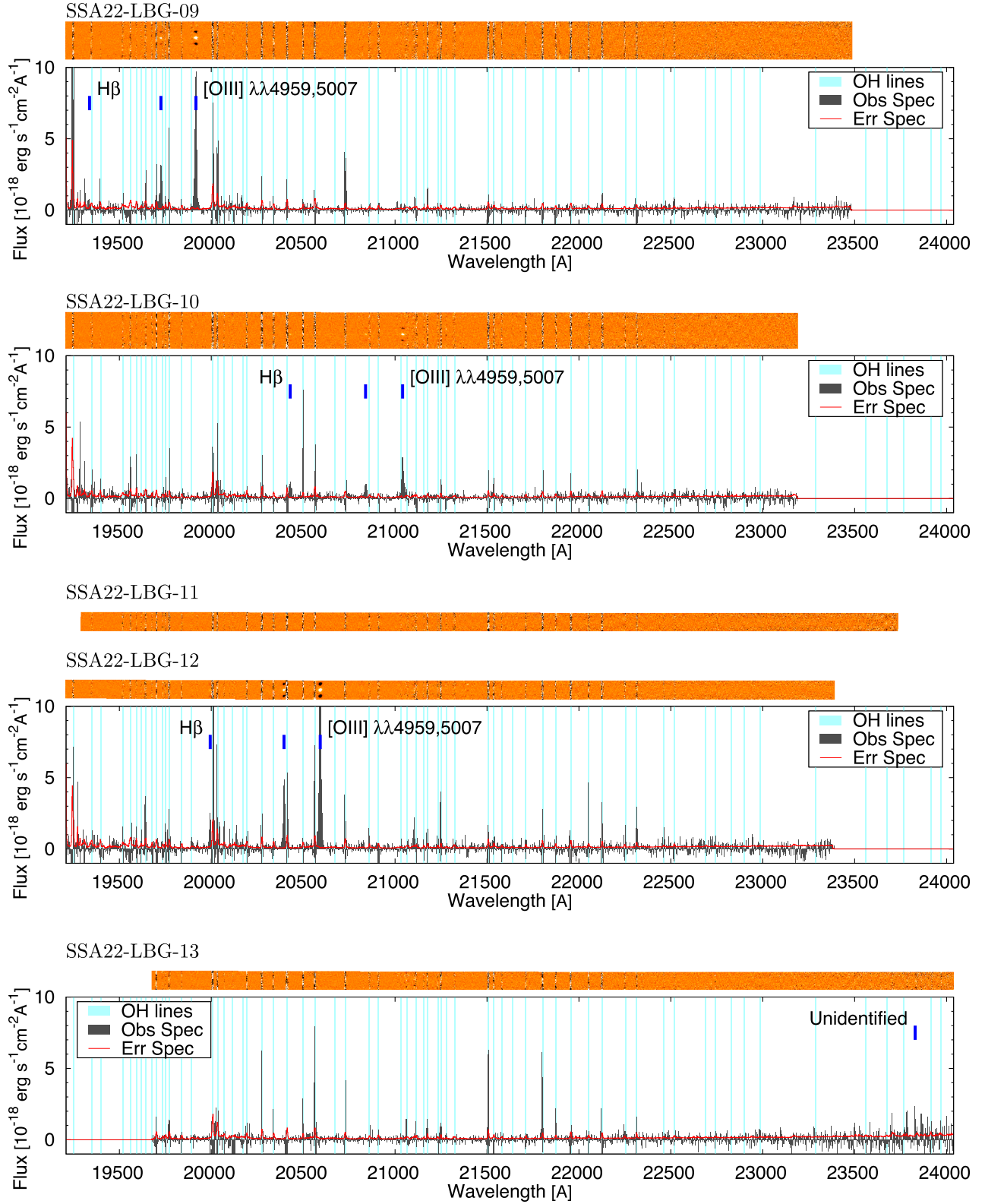
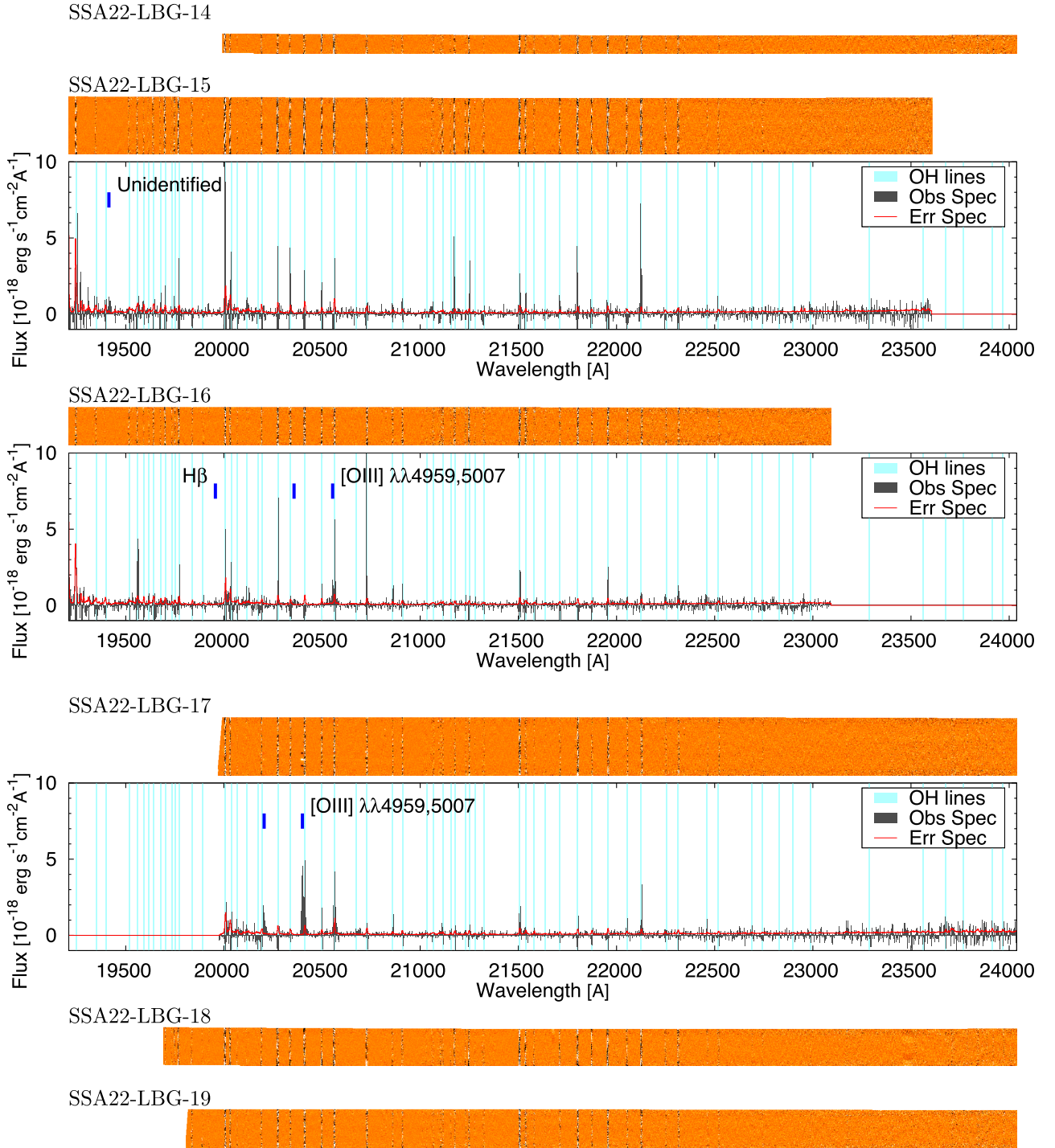
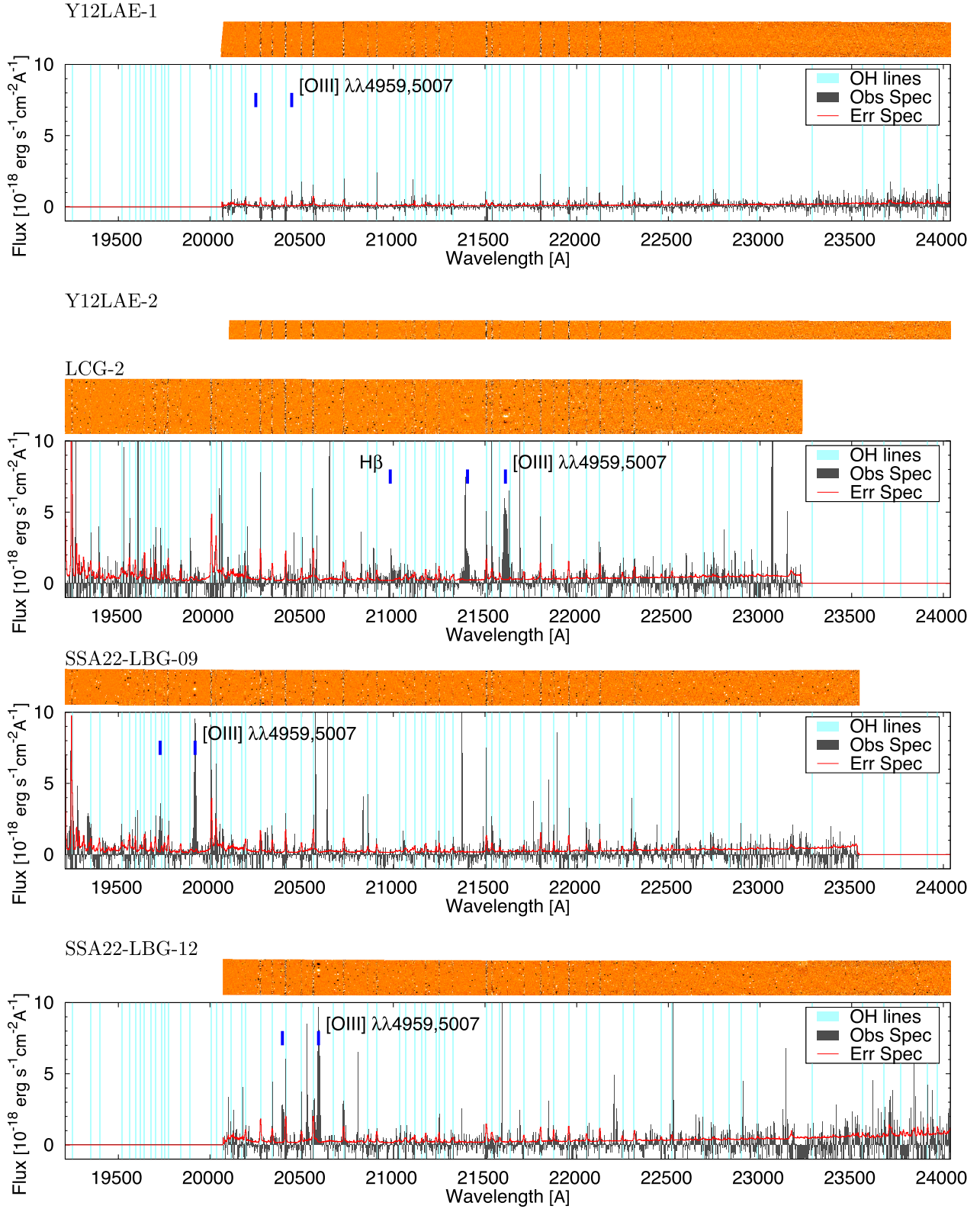


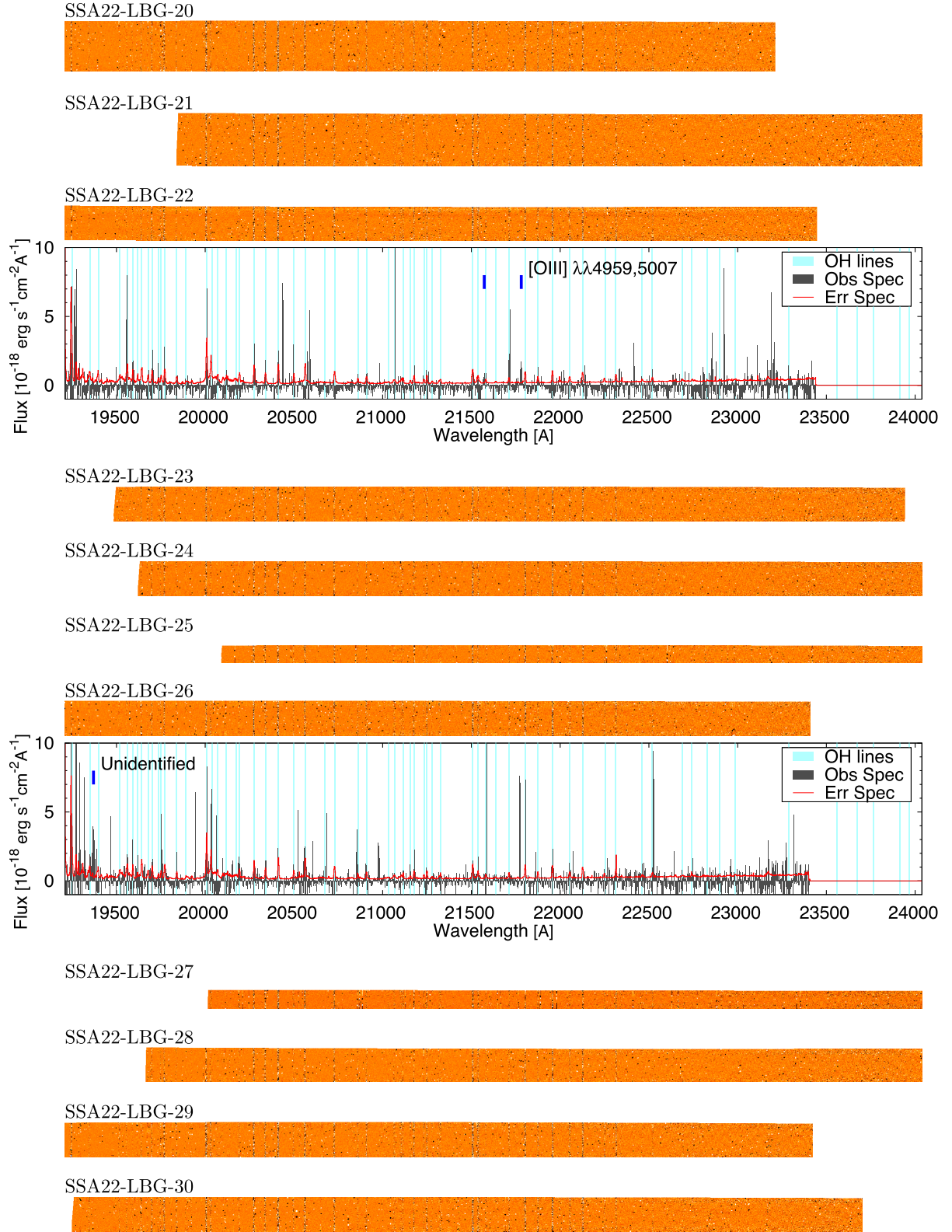
Figure A1. Reduced 2D images and 1D spectra. The detected lines are marked by blue thick lines.

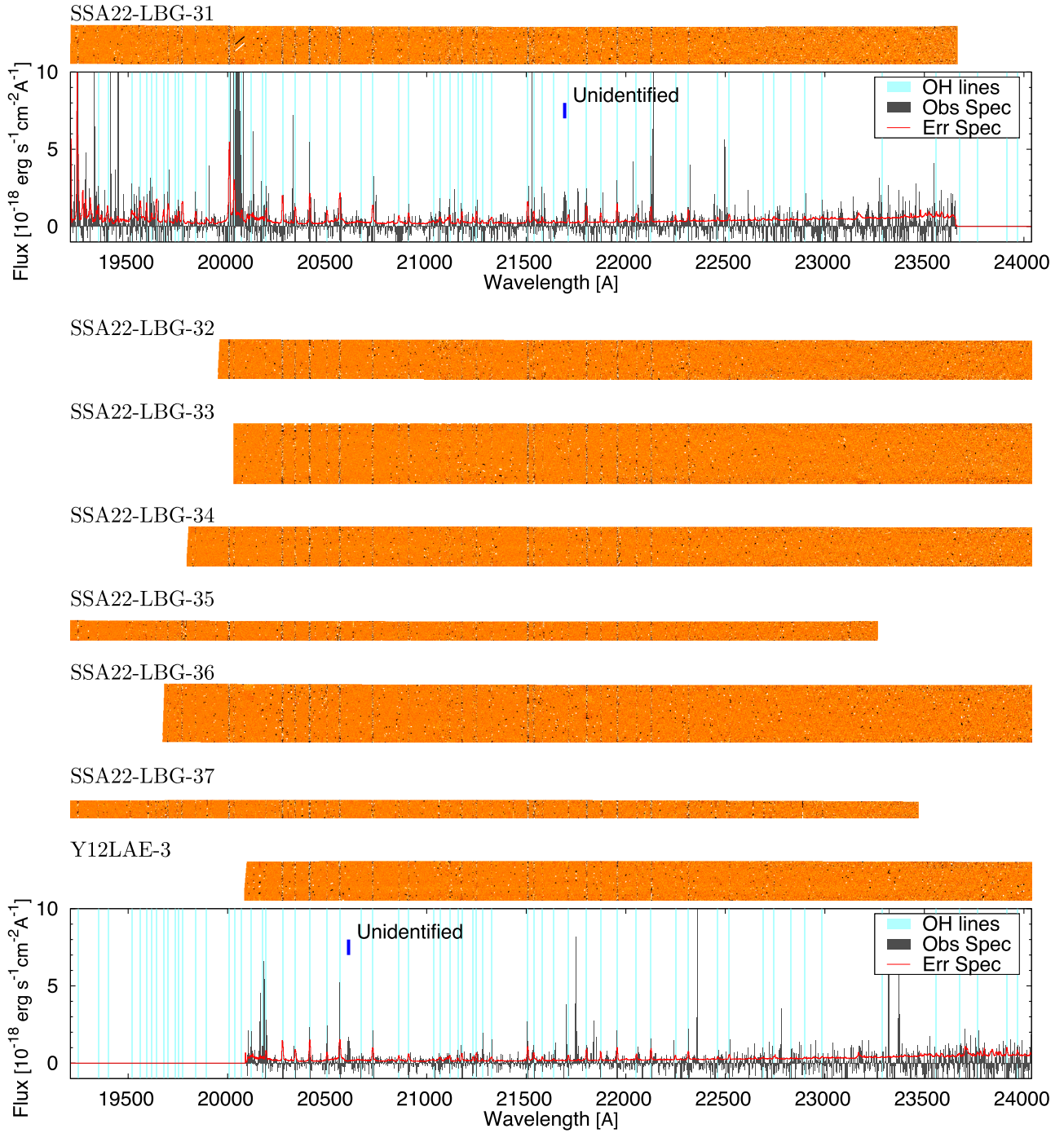
Figure A1. *Continued*

Figure A1. *Continued*

Figure A1. *Continued*

Figure A1. *Continued*

Figure A1. *Continued*

Figure A1. *Continued*

This paper has been typeset from a \LaTeX file prepared by the author.